IONOSPHERE INTERPOLATION FOR UNDIFFERENCED AND UNCOMBINED PPP-RTK IN HONG KONG

CHEN DINGYUAN

MPhil

THE HONG KONG POLYTECHNIC UNIVERSITY

2025

The Hong Kong Polytechnic University

Department of Aeronautical and Aviation Engineering

Ionosphere interpolation for undifferenced and uncombined PPP-RTK in hong kong

Chen Dingyuan

A thesis submitted in partial fulfilment of the requirements for the degree of Master of Philosophy

Dec 2024

CERTIFICATE OF ORIGINALITY

I hereby declare that this thesis is my own work and that, to the best of my knowledge and belief, it reproduces no material previously published or written, nor material that has been accepted for the award of any other degree or diploma, except where due acknowledgement has been made in the text.

_____(Signed)

CHEN Dingyuan (Name of student)

ABSTRACT

Precise point positioning–real-time kinematic (PPP-RTK) integrates the benefits of traditional positioning techniques RTK and PPP to provide fast and high-accuracy positioning, making it very ideal for the autonomous driving industry. Among PPP-RTK models, the Undifferenced an Uncombined (UDUC) PPP-RTK shows the capability to adeptly process multi-frequency and multi-GNSS data, demonstrating significant potential and possibilities. However, its positioning accuracy is influenced by numerous factors, particularly ionospheric delay. The PPP-RTK generates ionospheric delay corrections by the interpolation of reference stations. Therefore, it is imperative to identify an appropriate ionospheric interpolation technique to guarantee positioning accuracy. This thesis seeks to evaluate the interpolation accuracy and positioning performance of various current interpolation techniques, including Inverse Distance Weighted (IDW) method, Least Squares Collocation (LSC) method, Kriging method and Planar Fitting (PF) method, under quiet and moderate ionospheric conditions, aiming to figure out the most appropriate interpolation model for PPP-RTK in Hong Kong, which is in low-latitude regions with short inter-station distance. To achieve this objective, the author modifies the open-source MATLAB software PPPH and build up the UDUC PPP-RTK experimental platform for this thesis. Subsequently, the author resolves and analyzes the data from 16 stations within the Hong Kong reference station network. Numerical analysis shows that Universal Kriging method is the most appropriate interpolation technique for UDUC PPP-RTK in Hong Kong. This approach exhibits high interpolation accuracy and superior positioning performance in millimeter level, while also exhibiting better robustness among these methods.

KEYWORDS: UDUC PPP-RTK, Positioning in Hong Kong, Ionospheric delay, Interpolation models

ACKNOWLEDGEMENTS

First and foremost, I would like to express my deepest gratitude to my supervisor, Professor Jiang Yiping, for her invaluable guidance, patience, and support throughout my research journey at Hong Kong Polytechnic University. Her insights and expertise have been instrumental in shaping both the direction and success of my thesis.

I am also thankful to the faculty and staff of the Department, who have provided me with the resources and environment necessary for my academic pursuits. Their assistance has been a cornerstone of my research experience.

Additionally, I would like to extend my sincere thanks to the various global institutions that provided the critical data necessary for my research. Their willingness to share knowledge and resources has significantly enriched my study and contributed to the depth and breadth of my analysis.

My peers and fellow graduate students deserve special mention for their encouragement and constructive critiques that have greatly helped me refine my work.

Lastly, I would like to extend my appreciation to my family and friends, whose enduring support and understanding have been vital during my studies.

Thank you all for your contributions to my academic journey and for making this thesis possible.

TABLE OF CONTENTS

1. Introduction

1.1 Introduction to the PPP-RTK

Precise Point Positioning (PPP) was initially outlined in seminal works by Heroux and Kouba and Zumberge[1][2]. This method, which can achieve centimeter to decimeter accuracy, utilizes both code observations and carrier phase observations in just one single GNSS receiver. In order to accomplish this, accurate information such as precise satellite orbits and clocks products is crucial, usually generated and broadcast by the International GNSS Service and other external organizations [3]. However, the level of accuracy attainable with PPP is heavily reliant on the duration of observation. For instance, single-frequency PPP cannot form ionosphere-free observation combinations to eliminate ionospheric delays. Hence, it depends on ionospheric corrections provided from external data such as Global Ionospheric Maps [4-6], in which case it achieves a positioning accuracy of several decimeters after approximately 15 minutes [7]. Even though single-frequency PPP can also attain accuracy at the centimeters level by utilizing dual-frequency observations without Global Ionospheric Maps, it requires significantly longer observation periods with a minimum duration of one hour [8][9].

In contrast to code observation data, the carrier phase observation data utilized in PPP is much more precise. However, it still faces difficulties in integer ambiguity resolution. When it comes to relative positioning techniques like Real-time Kinematic (RTK), they allow for double-difference calculation of carrier-phase ambiguities, which is of vital importance to integer ambiguity search. This enables accurate positioning performance ranging from millimeters to centimeters, utilizing the exactness of the phase data. Several advanced methods have been presented to tackle the essential problem of resolving integer ambiguities, with the Least-Square Ambiguity Decorrelation Adjustment (LAMBDA) technique emerging as the established benchmark [10]. However, the quick fix of integer ambiguities is only feasible at distances shorter than ten kilometers between the user side and the server side, assuming that changes in ionospheric delays are insignificant.

Over the past ten years, many scholars have developed several methods that enable integer ambiguity resolution in PPP. For an in-depth analysis, the goal of these techniques is to achieve

accuracy comparable to RTK by resolving phase ambiguities within observations from a solitary receiver, refer to Teunissen and Khodabandeh [11]. This involves the incorporation of data regarding satellite phase and code biases [12-16]. Consequently, PPP can also be regarded as a relative positioning approach since the corrections for orbit, clock, and hardware biases are sourced from a network of global or regional reference receivers[17].

Recently, as an extension of PPP method, a novel method called PPP-RTK is gaining popularity in schools and labs. It combines the benefits of both PPP and RTK methods, which can achieve fast ambiguity resolution in one single receiver using corrections generated by reference stations and analysis centers [18]. The duration of convergence for PPP-RTK is comparable to RTK and far less than PPP, while yet achieving accuracy at the centimeter level. Conversely, PPP-RTK is not constrained by the duration of the baseline data, unlike RTK. Reference stations ranging from tens of kilometers to hundreds of kilometers can all contribute to the positioning solutions. Furthermore, the RTK approach incorporates the Observation Space Representation (OSR) corrections. That is to say, the reference stations transmit the aggregate value of all GNSS error sources to the consumers. In contrast to OSR, PPP-RTK employs State Space Representation (SSR) corrections, allowing for the identification of various correction for distinct sources of errors, for instance satellite clock error, atmospheric delays, and satellite orbit error. Through this method, SSR corrections notably lessen the communication load, thus enabling support for a large number of users [19][20]. Moreover, GNSS-related errors, which vary in time and space, can be distinctly represented, thereby enhancing the potential for improved positioning accuracy. As a result, PPP-RTK can provide comparable RTK-like accuracy and performance, while offering a longer operational range, diminished communication requirements, and enhanced error resilience. This renders it a promising technique for autonomous driving and UAV, as seen in Figure 1.1 [21].

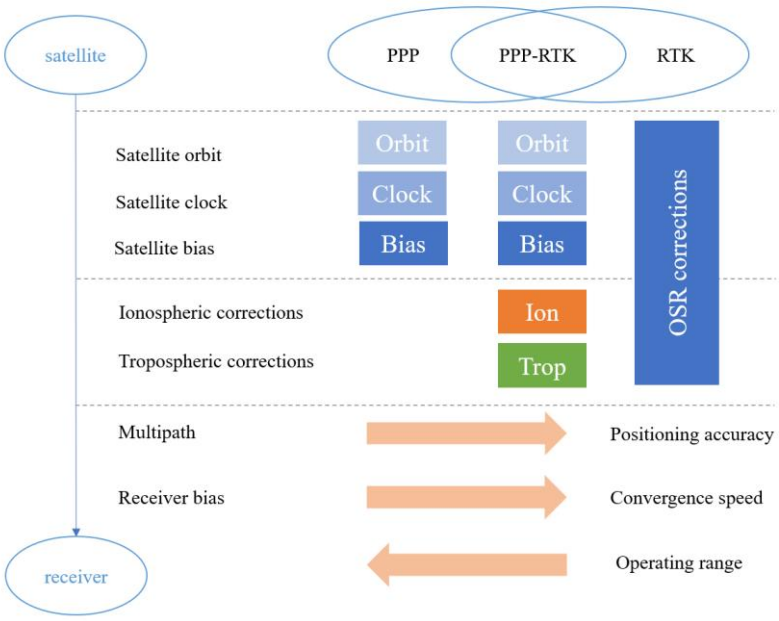

Figure 1.1 Comparison of PPP, RTK and PPP-RTK

The PPP-RTK consists of two stages: the server side and the user side [22]. At first, the network of reference stations analyzes GNSS data to produce various corrections as the server side [23]. These corrections include the satellite code and phase bias, satellite clock and orbit error [24][25]. In addition, if the network is small- or medium-scale, the slant ionospheric delay will be calculated as the input data of interpolation for the user side [26][27]. After that, the user side will receive these corrections generated and broadcast by the network, therefore making it possible to achieve fast ambiguity resolution. The schematic representation of a PPP–RTK system is seen in Figure 1.2.

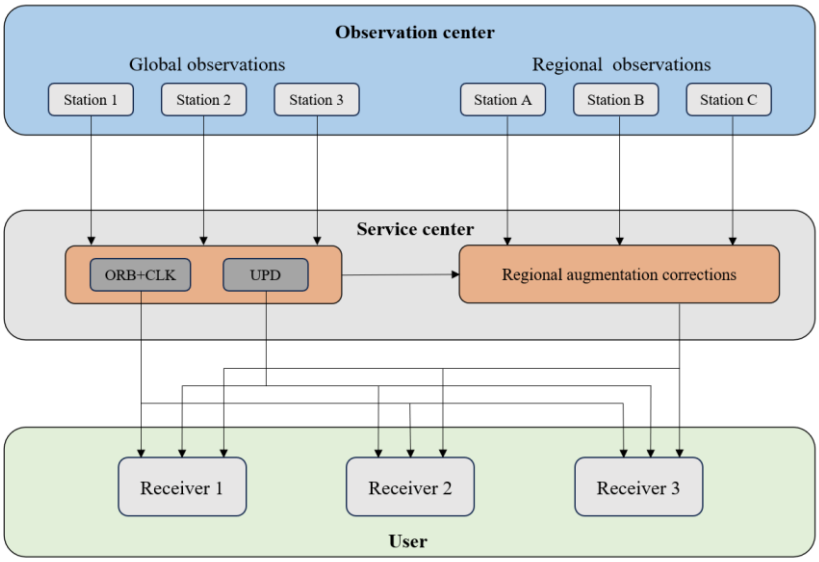

Figure 1.2 General flow of PPP-RTK system [21]

At present, several kinds of PPP-RTK methods have been proposed and each of the functional model has been formulated. Based on numbers of frequencies and systems, PPP-RTK can be categorized into single-frequency and multi-frequency models, such as single-system PPP-RTK and dual-frequency PPP-RTK [28-34]. Based on the distance of reference stations, previous studies proposed three PPP-RTK models, among which are Ionosphere-Float, Ionosphere-Weighted and Ionosphere-Fix PPP-RTK [35-38]. As the distances between reference stations grow shorter, the spatial correlation of ionospheric delay and its constraint increase [39]. Besides, based on the combination and differentiation of observations, researchers have proposed ionosphere-free model and undifferenced and uncombined model. While the former model combines observations of two frequencies to eliminate ionospheric delay [40-43], the latter model does not make any combination or difference. Details of their advantages and disadvantages will be presented in Section 1.2.

1.2 Introduction to the Undifferenced and Uncombined Model

In previous studies, differentiation of observation data is widely used to enhance the positioning performance [44-46]. The basic principle is making difference to eliminate common errors. There are various approaches of differentiation:

- Inter-station single difference: By making single difference between stations simultaneously observing the exact same satellite, the common errors of satellite are able to be almost eliminated. Furthermore, given that the baseline is generally modest in comparison to the height of the satellites, the atmospheric delays and orbit errors in two receivers are analogous [47]. Nonetheless, this relationship evidently diminishes when the distance lengthens [48].
- Inter-satellite single difference: By making single difference between satellites in same station, it is possible to eliminate receiver clock error. The atmospheric delays in two frequencies, such as ionospheric delay, are almost equal upon reaching the sole receiver, hence mitigating the impacts of ionospheric and tropospheric delays [49].
- Double difference: The double difference combines the two kinds of single difference above. It has effectively eradicated clock errors of both receivers and satellites, which is

utilized in the majority of GNSS post processing applications. However, we still need to deal with the ambiguity resolution in the carrier phase observation [50-54].

- Triple difference: The triple difference is the disparity between double difference and inter-epoch difference. Since it facilitates the detection and correction of cycle slip, triple differencing serves effectively as preliminary procedures.

In addition to differentiation, various combinations of GNSS measurement are also widely employed for diverse application:

- Ionosphere-free combination: This method combines measurements of two different frequencies to remove the first-order ionospheric delay as this parameter is related to GNSS signal's frequency. The remaining part of ionosphere affecting the positioning solutions corresponds to only a few centimeters or even less [55-57].
- Geometry-free combination: This approach facilitates the estimation or elimination of geometry, including clocks and all non-dispersive effects in the signal [58]. After combination, it contains ionospheric delays and all kinds of bias that are frequency-dependent such as hardware biases, cycle slips, and ambiguities [59].
- Wide-lane and narrow-lane combination: This method combines the carrier phase measurements of two individual frequencies, which keeps ambiguity integer. The large wavelength of wide-lane combination is advantageous for ambiguity resolution, cycle-slip identification, and outlier detection. [60]. But the noises present in original observations are also amplified [61]. On the contrary, the narrow-lane combination has lower noise than original observations while it makes it more difficult to ambiguity resolution in comparison to other combinations [62][63].

Despite its ability to reduce numerous sources of error and provide accurate positioning solutions, the process of constructing linear combinations of observations still has particular limitations. Linear combinations decrease the numbers of observations equations and increase the observation noise, which affects the accuracy and reliability of positioning. Furthermore, taking ionosphere-free model as example, the information about the ionosphere is mostly eliminated, which means that we are unable to obtain the ionospheric corrections. If we utilize the original observation data and do not make any difference and combinations, observation redundancy can be guaranteed and all of the parameters can be remained. This approach has

superior scalability and will not be constrained by the numbers of frequencies and systems employed in positioning solution. It is hence more suitable for the trend of multi-frequency and multi-system PPP-RTK.

Teunissen proposed the undifferenced and uncombined (UDUC) model initially and applied Singularity-basis (S-basis) theory for solving the rank deficiency of UDUC design matrix as UDUC model estimates all of parameters at the same time [64]. Then, Odijk et al. analyzes the estimability of parameters in UDUC PPP-RTK in detail [65]. They successfully identify the null space of matrix and provide the S-basis to choose corresponding to different situations of rank deficiency. Researchers subsequently expand the application of the undifferenced and uncombined PPP–RTK approach, originally utilized in dual-frequency GPS scenarios, to encompass both multi-frequency and multi-GNSS applications [66-70]. This update enables a wider and more adaptable incorporation of GNSS systems and frequencies, hence improving the reliability and precision of the positioning solutions. Based on the distances between reference stations in the network, Dimitrios and Sandra propose the Ionosphere-Float (IF) UDUC and Ionosphere-Weighted (IW) UDUC models [71][72], which constrain the ionospheric delay in different approaches, and evaluate the user performance using the corrections generated from the networks. Zhang et al. further develops a category of UDUC PPP-RTK models and formulate its function under each circumstance, such as Code Division Multiple Access signals and Frequency Division Multiple Access signals, PPP–RTK using code and carrier-phase measurements and PPP–RTK using carrier-phase measurement solely, IF UDUC and IW UDUC model [73]. Furthermore, the authors also systematically analyze the relationships and distinctions across different existing PPP-RTK models [74].

1.3 Problem Statement and Objectives

Though, plenty of undifferenced and uncombined PPP-RTK models have been proposed, few studies focus on the ionospheric correction generations. Ionospheric corrections generated by interpolation models are of vital importance of enabling fast ambiguity resolution in PPP-RTK. Choosing an appropriate interpolation method for different application areas of PPP-RTK can significantly enhance the accuracy of ionospheric corrections, and thus enhance the

positioning accuracy and integrity at the user end [75-78]. Therefore, it is imperative to compare and investigate different interpolation methods in certain area[79].

To predict the ionospheric delay, researchers have proposed plenty of interpolation methods. Bartier and Keller proposes the Inverse Distance Weighted (IDW) method to predict the ionospheric delay in the interpolated point [80]. This method is suitable for quick analysis and small-sized data sets but it is sensitive to outliers and lack of structural information. And Oliver proposes the Kriging method to improve the performance of interpolation for geographical systems [81]. Kriging method can consider spatial correlations in the interpolated zone and adjust the weights through the variogram model to reduce the errors. However, the method relies on the statistical assumptions and requires appropriate variogram models. What's more, Moritz proposes the Least-Square collocation method for geophysical use [82]. This method introduces random signal estimation theory, which can better estimate the characteristics of the interpolation area. But it is still sensitive to extreme anomalies. And Nurunnabi proposes the robust Planar Fitting (PF) method for data processing [83]. This method also can represent the trend of the interpolated zone and easy to process. However, similar to IDW method, this method is also sensitive to extreme conditions.

This thesis mainly focuses on the Hong Kong, which is in low-latitude regions with short inter-station distance and difficult to achieve high-accuracy positioning, to systematically investigate the performance of various interpolation methods with the aim of providing appropriate solutions for PPP-RTK and proposing robust mitigation techniques. Given Hong Kong's geographical location at low latitude and the average distance between reference stations that is in the range of tens of kilometers, we utilize Ionosphere-Weighted UDUC PPP-RTK models and choose approximately 16 reference stations as the network to extract the ionospheric delays. Next, various current and classic interpolation models, such as the IDW method, PF method and Kriging method, are used to produce the ionospheric corrections on the user side. Along with other received corrections, the user side can estimate its position using different kinds of ionospheric corrections respectively. Finally, we compare and analyze the positioning accuracy in various circumstances to propose the most suitable method in Hong Kong.

1.4 Outline of This Thesis

This thesis is organized as follows:

Chapter 2 introduces the basic method of UDUC PPP-RTK data processing. At first, S-basis theory is introduced to illustrate the principle of eliminating rank deficiency. Then, this chapter introduces the error sources and their correction models in GNSS, including the atmospheric error, satellite orbit and clock error and other system errors. Finally, this chapter introduces the ambiguity resolution method adopted in this thesis.

Chapter 3 introduces the functional models of UDUC PPP-RTK adopted in this thesis, including the network functional model and the user functional model. Furthermore, this chapter presents the adaptive extended Kalman filter as the estimator for the PPP-RTK state vectors. Finally, various interpolation techniques used for generating ionospheric correction are introduced in detail.

Chapter 4 introduces the experiments and provides a comprehensive analysis of obtained results. At first, the software platform and preparations for experiments are illustrated. Then, the performances of different techniques are evaluated and compared based on the accuracy of user positioning solutions. At last, this chapter discusses the findings of the experiments and draws the conclusions.

Chapter 5 provides a concise summary and review of the whole thesis. Furthermore, this chapter highlights the constraints of UDUC PPP-RTK and methods for generating corrections, and provides suggestions for future researches.

2. Error Processing Theory of UDUC PPP-RTK Data

This chapter introduces the processing theories for various errors of UDUC PPP-RTK model, including rank deficiencies elimination, tropospheric delay modelling, ambiguity resolution.

2.1 Singularity-basis Theory and Null-space Identification

2.1.1 Review of S-basis theory

Equation (2.1.1) generally specifies the linearized model of observation equations as [23]:

$$E\{y\} = Ax \tag{2.1.1}$$

$E\{\cdot\}$ represents the expectation, x is n-th unknown parameter vector. y denotes the m-th observation vector. $R(\cdot)$ is the range or column space. A denotes the $m \times n$ design matrix with rank r that is less than n. This indicates A is not full ranked with the deficiency quantified as $dimN(A) = n - r$. The $N(A)$ denotes the null space of A. Assuming the matrix V which is $n \times (n-r)$ order to be the basis, we can infer that $AV = 0$, for $N(A) = R(V)$. $R(V)$ is sole, nevertheless, the V, which consists of the basis vectors across the null space, isn't as sole as $R(V)$.

This means that A is not full ranked and it is unfeasible to resolve all of the unidentified parameters. Therefore, we divide vector x into two parts, the estimable part denoted as $\tilde{x}_s \in R(S)$, and an inestimable part designated as $x_v \in R(V)$, where S and V are basis matrices with equivalent spaces, in other word, $R_n = R(S) \oplus R(V)$

$$x = \underbrace{S\tilde{\alpha}}_{\tilde{x}_s} + \underbrace{V\beta}_{x_v} = \underbrace{[S \quad V]}_{n \times n}\begin{bmatrix}\tilde{\alpha}\\ \beta\end{bmatrix} \tag{2.1.2}$$

Where $\tilde{\alpha}$ represents the r-th estimable parameter. S denotes $n \times r$ matrix associated with $\tilde{\alpha}$. β signifies the $(n-r)$-th inestimable parameter. V represents the $n \times (n-r)$ null matrix. And selections of S are not singular and determine estimable parameters to be resolved. Figure 2.1 illustrates two kinds of decomposition, labeled S and S'. Therefore, we can determine that $R(S) \neq R(S')$.

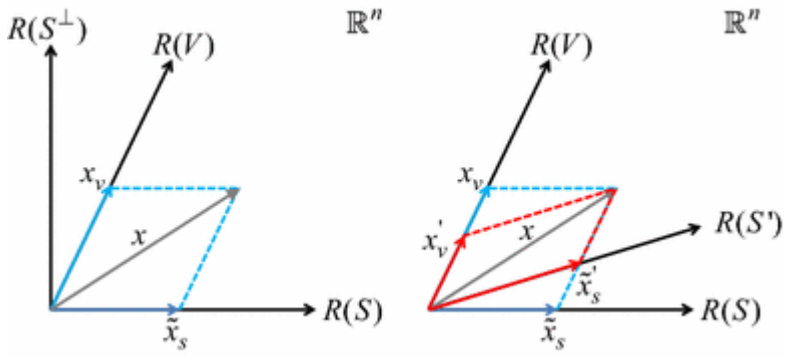

Figure 2.1 Two options for decomposing the parameter vector x: the estimable component $\tilde{x_s}$ and inestimable component x_v on the left, and estimable component $\tilde{x_s}'$ and inestimable component x_v' on the right

Given that the n-th matrix $[S\ V]$ is an invertible square matrix, we can solve $\tilde{\alpha}$ and β using Equation (2.1.3) [84]:

$$\begin{bmatrix}\tilde{\alpha}\\ \beta\end{bmatrix} = [S\ \ V]^{-1}x = \begin{bmatrix}[(V^{\perp})^T S]^{-1}(V^{\perp})^T\\ [(S^{\perp})^T V]^{-1}(S^{\perp})^T\end{bmatrix}x \tag{2.1.3}$$

$(\cdot)^T$ represents the transpose. And $V^{\perp}$ denotes the $n \times r$ matrix satisfying that $(V^{\perp})^T V = 0$. Vector β denotes the minimum constraints vector. The $n \times (n-r)$ matrix $S^{\perp}$ serves as a basis for $R(S)$, satisfying that $(S^{\perp})^T S = 0$.

The full-rank matrix $\tilde{\alpha}$ is derived by inserting $x = S\tilde{\alpha} + V\beta$ into Equation (2.1.1):

$$E\{y\} = Ax = A(S\tilde{\alpha} + V\beta) = \underbrace{(AS)}_{\tilde{A}}\tilde{\alpha} \tag{2.1.4}$$

Thus, the design matrix is full ranked as rank deficiency is eliminated. With Equation (2.1.2), the estimable part can be computed as:

$$\tilde{x}_s = S\tilde{\alpha} = x - V\beta = \mathcal{S}x \tag{2.1.5}$$

Where S represents the n-th S-transformation square matrix, calculated by utilizing Equation (2.1.3), as:

$$\mathcal{S} = S[(V^{\perp})^T S]^{-1}(V^{\perp})^T = I_n - V[(S^{\perp})^T V]^{-1}(S^{\perp})^T \tag{2.1.6}$$

Another choice is shown as the right part of Figure 2.1, and the corresponding transformation matrix is:

$$\tilde{x}_s' = S'\tilde{\alpha}' = x - V\beta' = \mathcal{S}'x \tag{2.1.7}$$

And S' is computed as:

$$\begin{aligned} S' &= S'[(V^{\perp})^T S']^{-1}(V^{\perp})^T \\ &= I_n - V[(S'^{\perp})^T V]^{-1}(S'^{\perp})^T \end{aligned} \tag{2.1.8}$$

2.1.2 Null-space Identification in UDUC PPP-RTK

The GNSS original equations are shown in Equation (2.1.9), where *i* denotes epoch with *i* = 1, . . . k, *r* denotes the receiver with *r* = 1, . . . n, *s* denotes the satellite with *s* = 1, . . . m. *j* denotes the frequency with *j* = 1, . . . f [85][86].

$$\begin{cases} E(\Delta p_{r,j}^s(i)) = c_r^s(i) \cdot \Delta x_r(i) + \mathrm{c}[dt_r(i) - dt^s(i)] + \\ \qquad g_r^s(i) \cdot \tau_r(i) + \mu_j l_r^s(i) + d_{r,j} - d_j^s \\ E(\Delta \phi_{r,j}^s(i)) = c_r^s(i) \cdot \Delta x_r(i) + c[dt_r(i) - dt^s(i)] + \\ \qquad g_r^s(i) \cdot \tau_r(i) - \mu_j l_r^s(i) + \delta_{r,j} - \delta_j^s + \lambda_j N_{r,j}^s \end{cases} \tag{2.1.9}$$

Here $\Delta\Phi_{r,j}^s$ denotes the UDUC observed-minus-computed (OMC) carrier-phase measurements and $\Delta p_{r,j}^s$ denotes the OMC pseudorange measurements. $\Delta x_r(i)$ denotes the increment vector of receiver positions in three directions and c_r^s denotes the unit vector whose direction is from receiver to satellite. dt_r denotes the clock error of receiver and dt_s denotes the satellite clock error. $d_{r,j}$ and d_j^s denote the instrument code bias of receiver and satellite and *б* denotes the instrument phase bias. l_r^s denotes the first-order ionospheric delay and μ_j denotes f_1^2/f_j^2. N denotes the ambiguities and λ denotes the wavelength of carrier phase in each frequency. T_r denotes the tropospheric wet component delay. g_r^s denotes the mapping function.

Then, we combine Equation (2.1.9) with Kalman filter. The observation model and the dynamic model of Kalman filter is:

$$\begin{aligned} \Delta y_i &= A_i \Delta x_i + l_i, i = 1, ..., k \\ \Delta x_i &= \Phi_{i,i-1} \Delta x_{i-1} + w_i, i = 2, ..., k \end{aligned} \tag{2.1.10}$$

Here *A* denotes the design matrix containing the coefficients in Equation (2.1.9) such as light speed, mapping function and wavelength. *Y* denotes the vector of observed-minus-computed measurement and x_i denotes the state vector containing the unknown parameters in every epoch. *Φ* denotes the transition matrix connecting one epoch with the next. l_i and w_i denotes the measurement and process noise following the zero-mean Gaussian distribution. Therefore, we can rewrite Equation (2.1.10) as

$$\begin{bmatrix} E\{\Delta y\} \\ 0 \end{bmatrix} = \begin{bmatrix} A \\ B \end{bmatrix} E\{\Delta x\} \tag{2.1.11}$$

Where

$$A = blkdiag(A_1, ..., A_k), \quad B = [B_2^T, ..., B_k^T]^T \tag{2.1.12}$$

The design matrix $[\ A^{\mathrm{T}}\ B^{\mathrm{T}}]^{\mathrm{T}}$ determines rank inadequacy. Next, following the order of carrier phase measurement, code measurement and random parameters, the rank-deficient matrix can be succinctly expressed as [23]:

$$A_{net} = [\ A_{geo} \quad A_{rec} \quad A_{sat} \quad A_{ion} \quad A_{amb}\ ] \tag{2.1.13}$$

Where

$$A_{geo} = \begin{bmatrix} F_{geo} \\ D_k^T \otimes (I_n \otimes I_\nu) \\ 0 \\ 0 \\ 0 \end{bmatrix} \tag{2.1.14}$$

$$A_{rec} = \begin{bmatrix} I_k \otimes \left\{ \begin{pmatrix} e_f & \Lambda & 0 \\ e_f & 0 & I_f \end{pmatrix} \otimes (I_n \otimes e_m) \right\} \\ 0 \\ D_k^T \otimes \left\{ \begin{pmatrix} 1 & 0 & 0 \\ 0 & I_f & 0 \\ 0 & 0 & I_f \end{pmatrix} \otimes I_n \right\} \\ 0 \\ 0 \end{bmatrix} \tag{2.1.15}$$

$$A_{sat} = \begin{bmatrix} I_k \otimes \left\{ \begin{pmatrix} e_f & \Lambda & 0 \\ e_f & 0 & I_f \end{pmatrix} \otimes (-e_n \otimes I_m) \right\} \\ 0 \\ 0 \\ D_k^T \otimes \left\{ \begin{pmatrix} 1 & 0 & 0 \\ 0 & I_f & 0 \\ 0 & 0 & I_f \end{pmatrix} \otimes I_m \right\} \\ 0 \end{bmatrix} \tag{2.1.16}$$

$$A_{ion} = \begin{bmatrix} F_{ion} \\ 0 \\ 0 \\ 0 \\ D_k^T \otimes I_m \end{bmatrix} \tag{2.1.17}$$

$$A_{amb} = \begin{bmatrix} e_k \otimes \left\{ \begin{pmatrix} \Lambda \\ 0 \end{pmatrix} \otimes (I_n \otimes I_m) \right\} \\ 0 \\ 0 \\ 0 \\ 0 \end{bmatrix} \tag{2.1.18}$$

Table 2.1 delineates the exact definitions of the elements utilized in aforementioned matrix. As illustrated in Equation (2.1.13), the sections in the first row of the design matrix are dedicated to phase and code observables and the lower section addresses the random-walk constraints. The design matrix's structure, associated with particular parameter sets, is delineated in the following order: The first group A_{geo} comprises the coordinates of receivers along with Zenith Total Delays. The subsequent group A_{rec} encompasses hardware biases and clocks, which are related to receivers. The next set A_{sat} includes the clocks and hardware biases which are related to the satellites. The fourth group A_{ion} includes the ionospheric delay and the last group A_{amb} is designated for ambiguities.

Table 2.1 Explanations of commonly used scalars, vectors and matrices

Symbol	Definition	Symbol	Definition
k	= # epochs	$e_{(\cdot)}$	$= (1, 1, \ldots, 1)^T$
f	= # frequencies	$I_{(\cdot)}$	$= \mathrm{diag}(1, 1, \ldots, 1)$
n	= # receivers	$D^T_{(\cdot)}$	$= [-e_{(\cdot)-1} \;\; I_{(\cdot)-1}]$
m	= # satellites	μ	$= (\mu_1, \mu_2, \ldots, \mu_f)^T$
v	= # geometry comp.	Λ	$= \mathrm{diag}(\lambda_1, \lambda_2, \ldots, \lambda_f)$
$c_{(\cdot)}$	$= (1, 0, \ldots, 0)^T$	$C_{(\cdot)}$	$= \begin{bmatrix} 0_{1\times\{(\cdot)-1\}} \\ I_{(\cdot)-1} \end{bmatrix}$

Having divided the unknown parameters into five parts, the rank deficiency is also classified into five corresponding situations. Denoted as V_{net}, by utilizing the subsequent construction procedure, one can get the basis matrix as follows [23]:

$$V_{net} = [V_1 \;\; V_2 \;\; V_3 \;\; V_4 \;\; V_5] \tag{2.1.19}$$

Where

$$V_1 = \begin{bmatrix} 0 \\ e_k \otimes \left\{ \begin{pmatrix} 1 & 0 & 0 \\ 0 & I_f & 0 \\ 0 & 0 & I_f \end{pmatrix} \otimes e_n \right\} \\ e_k \otimes \left\{ \begin{pmatrix} 1 & 0 & 0 \\ 0 & I_f & 0 \\ 0 & 0 & I_f \end{pmatrix} \otimes e_m \right\} \\ 0 \\ 0 \end{bmatrix} \tag{2.1.20}$$

$$V_2 = \begin{bmatrix} 0 \\ 0 \\ e_k \otimes \left\{ \begin{pmatrix} \Lambda^{-1} e_f \\ e_f \end{pmatrix} \otimes C_n \right\} \\ 0 \\ 0 \\ 0 \end{bmatrix} \tag{2.1.21}$$

$$V_3 = \begin{bmatrix} 0 \\ 0 \\ e_k \otimes \left\{ \begin{pmatrix} -1 \\ \Lambda^{-1} e_f \\ e_f \end{pmatrix} \otimes I_m \right\} \\ 0 \\ 0 \end{bmatrix} \tag{2.1.22}$$

$$V_4 = \begin{bmatrix} 0 \\ e_k \otimes \left\{ \begin{pmatrix} 0 \\ I_f \\ 0 \end{pmatrix} \otimes -C_n \right\} \\ 0 \\ 0 \\ I_f \otimes (C_n \otimes e_m) \end{bmatrix} \tag{2.1.23}$$

$$V_5 = \begin{bmatrix} 0 \\ 0 \\ e_k \otimes \left\{ \begin{pmatrix} 0 \\ I_f \\ 0 \end{pmatrix} \otimes I_m \right\} \\ 0 \\ I_f \otimes (e_n \otimes I_m) \end{bmatrix} \tag{2.1.24}$$

According to Equation (2.1.19) – (2.1.24), we can classify the rank deficiencies into five cases with corresponding null space matrix as shown in Table 2.2. It should be noted

that case 1 and case 2 pertain to the same scenario, both belonging to a rank insufficiency between the satellite-related term and the receiver-related term.

Table 2.2 Number of rank deficiency in various cases

Null Space Matrix	Cases	Number of rank deficiency
V_1	Receiver and satellite clock	1
	Receiver and satellite hardware bias	$2f$
V_2	Receiver clock and receiver hardware bias	n-1
V_3	Satellite clock and satellite hardware bias	m
V_4	Receiver hardware bias and ambiguity	f*(n-1)
V_5	Satellite hardware bias and ambiguity	f*m

2.2 Tropospheric Delay Modeling

Troposphere is part of the atmosphere which has an attitude range of around 13 kilometers. When travelling through it, the GNSS signals is subject to interference, resulting in an additional delay as known as tropospheric delay. Tropospheric delays are contingent upon pressure, temperature, humidity, and the locations of antennas. Therefore, it has no correlation with frequency and we cannot mitigate this kind of error by any forms of combinations and differences. To deal with this problem, researchers develop several models for the tropospheric delay by considering various factors such as height, humidity, and pressure.

In general, most of tropospheric delay model divide this into two parts, the hydrostatic component delay and wet component delay. The former one caused by the dry gases is the majority of tropospheric delay, which usually accounts for 90%. This part of delay is quite stable and easy to model. While the latter one caused by water vapor is smaller but varies faster, which poses a significant challenge in tropospheric delay modeling. Consequently, the

hydrostatic delay is mitigated utilizing various standard models, whilst the wet delay is characterized as an indeterminate variable accompanied with stochastic noise. This section provides a review of various models frequently utilized by researchers.

2.2.1 Saastamoinen Model

By employing the latitude of the station, the air temperature, atmospheric pressure and water vapor pressure, this tropospheric delay model was proposed by Saastamoinen is able to determine the ZTD. This model is based on meteorological factors. Following is an illustration of the calculation formula that is used in the Saastamoinen model [87]:

$$\mathrm{ZTD} = \frac{0.0022768}{1 - 0.00266\cos(2\varphi)}\left(P + \left(\frac{1255}{T}\right)e\right) \tag{2.2.1}$$

Where φ is the latitude of stations in radius, P denotes the atmospheric pressure of the station. T denotes the Kelvin temperature. H denotes its ground elevation. e denotes the station's water vapor pressure.

2.2.2 GPT2w Model

The GPT2w model is developed based on empirical tropospheric data obtained from ECMWF. The variables considered are atmospheric pressure, air temperature, water vapor pressure, air temperature lapse rate, coefficients of the mapping function, the rate of water vapor breakdown and weighted mean atmospheric temperature. It takes into account both the yearly and semi-annual periods of the related parameters concurrently. Presented below is the model expression [88]:

$$\begin{aligned} a = a_0 + A_1\cos\left(\frac{\mathrm{doy}}{365.25}2\pi\right) + B_1\sin\left(\frac{\mathrm{doy}}{365.25}2\pi\right) + \\ A_2\cos\left(\frac{\mathrm{doy}}{365.25}4\pi\right) + B_2\sin\left(\frac{\mathrm{doy}}{365.25}4\pi\right) \end{aligned} \tag{2.2.2}$$

where a represents a parameter being assessed, a_0 denotes the average value, A_1 and B_1 denotes annual period coefficients, A_2 and B_2 denote semi-annual period coefficients. doy refers to the date.

Additionally, the GPT2w model employs two kinds of grids for representing the global area, whose resolutions are 5° × 5° and 1° × 1°, wherein the earth is partitioned by the grids.

When calculating, this model firstly computes the parameters where the points in the grid are surrounding the estimated point and then executes bilinear interpolation to derive the delays in the estimated point. Upon the computation of atmospheric temperature, the total tropospheric delay is divided into two parts, the zenith hydrostatic delay (ZHD) and the zenith wet delay (ZWD). And they are ascertained by Saastamoinen model and AN model respectively in GPT2w model as delineated in the subsequent formula.:

$$\mathrm{ZWD} = 10^{-6}\left(k_2' + \frac{k_3}{T_m}\right)\frac{R_d}{(\lambda+1)\,g_m}e_s \tag{2.2.3}$$

where k_2' and k_3 denote atmospheric refractive index constants. k_2' is set as 16.529 k·mb^{-1} and k_3 is set as 3.776 × 105 k·mb^{-1} respectively. T_m denotes the weighted mean atmospheric temperature. g_m denotes the gravitational acceleration. e_s denotes the water vapor pressure. R_d denotes the gas constant of dry air which is set as 287.058 J·kg^{-1}·K^{-1}. λ is determined by Equation (2.2.4):

$$\frac{e}{e_0} = \left(\frac{P}{P_0}\right)^{\lambda+1} \tag{2.2.4}$$

Equation (2.2.4) necessitates the alignment of meteorological contour data. Simply said, ZTD is the same as the aggregate of ZHD and ZWD. Consequently, GPT2w is able to produce empirical ZTD according to every specified time and location as an empirical model.

2.3 Ambiguity Resolution Technique

Having received all the corrections generated by the network and observation data broadcast by the satellites, the user side of UDUC PPP-RTK adopts Least-squares AMBiguity Decorrelation Adjustment (LAMBDA) method for ambiguity resolution [89]. The GNSS models on which ambiguity resolution is based, can all be cast in the following conceptual frame of linearized observation equations:

$$y = Aa + Bb + \epsilon \tag{2.3.1}$$

Where a is the integer parameter vector. b is the actual parameter vector, encompassing baseline components and potentially tropospheric and ionospheric delay, etcetera. A and B are defined as the coefficient matrices with $[A\ B]$ possessing full column rank. The observation

vector y contains the observed-minus-computed code and carrier-phase observables, which is contaminated by the random noise vector ϵ. The issues statement can be shown as:

$$\min_{a,b} ||y - Aa - Bb||^2_{Q_v} \tag{2.3.2}$$

Where $||\cdot||^2_Q = (.)^T Q_y^{-1}(.)$ and Q_y variance-covariance matrix of observations.

Equation (2.3.2) expressed above is a mixed integer least squares problem that can be solved by orthogonal decomposition:

$$||y - Aa - Bb||^2_{Q_v} = ||\hat{e}||^2_{Q_v} + ||\hat{b}(a) - b||^2_{Q_{\hat{b}(a)}} + ||\hat{a} - a||^2_{Q_{\hat{a}}} \tag{2.3.3}$$

Where $\hat{a}$ and $\hat{b}$ denote the unconstrained least square solution while $\breve{a}$ and $\breve{b}$ denote the integer solution.

This section will present the LAMBDA approach, organized in the sequence of float solution, followed by solving the decorrelation matrix and integer ambiguity search.

2.3.1 Float Solution

To get the float solution, Equation (2.3.1) can be transformed to:

$$\begin{bmatrix} B^T Q_y^{-1} B & B^T Q_y^{-1} A \\ A^T Q_y^{-1} B & A^T Q_y^{-1} A \end{bmatrix} \begin{bmatrix} b \\ a \end{bmatrix} = \begin{bmatrix} B^T Q_y^{-1} y \\ A^T Q_y^{-1} y \end{bmatrix} \tag{2.3.4}$$

Furthermore, Equation (2.3.3) can be expressed as:

$$\underbrace{\begin{bmatrix} N_a & N_{ba} \\ N_{ab} & N_a \end{bmatrix}}_{N} \begin{bmatrix} b \\ a \end{bmatrix} = \underbrace{\begin{bmatrix} r_b \\ r_a \end{bmatrix}}_{r} \tag{2.3.5}$$

Where N is dissolved via Cholesky Factorization.

Forward and backward substitution are the methods that are utilized to acquire the float solution. The ambiguity vector, the baseline vector, and the variance covariance matrix of float ambiguities are the parameters that make up the float solution.

$$\begin{bmatrix} \hat{b} \\ \hat{a} \end{bmatrix}, \begin{bmatrix} Q_{\hat{b}} & Q_{\hat{b}} \\ Q_{\hat{a}\hat{b}} & Q_{\hat{a}} \end{bmatrix} \tag{2.3.6}$$

2.3.2 Decorrelation Technique

Due to the correlation among float ambiguities, changes in one ambiguity parameter can impact the search for other ambiguities, significantly increasing the computational load of the

search algorithm. If reducing the correlation between ambiguity parameters, thereby minimizing the impact of changes in one ambiguity on the values of others, the ambiguity resolution process could be greatly accelerated. LAMBDA adopts *Z*-transformation to address this problem. At first, this method decomposed the variance-covariance matrix as:

$$Q_a = LDL^T \tag{2.3.7}$$

Where L is the lower triangular matrix that associates the covariance of the float with the estimated ambiguities. D is the diagonal matrix among which the element denotes the conditional covariance of the float ambiguities.

Then, we use *Z*-transformation to minimize the elements in L by means of the integer Gauss Transformation. Then integer gauss transformation can be written as:

$$Z_{ij} = I - \mu e_i e_j^T \tag{2.3.8}$$

Here μ is an integer. Substituting Z_{ij} into L

$$\overline{L} = LZ_{ij} = L - \mu L e_i e_j^T \tag{2.3.9}$$

Therefore, each element of the two matrices can be expressed as:

$$\begin{gathered} \overline{l}_{kj} = l_{kj} - \mu l_{ki} \\ k = i, \ldots, n \end{gathered} \tag{2.3.10}$$

And we choose $\mu = l_{ij}$ to minimize l_{ij} with:

$$l_{ij} < \frac{1}{2} \quad , i > j \tag{2.3.11}$$

Then, we revise the elements in the diagonal matrix D in a decreasing order. The detailed illustration of decomposed covariance matrix is:

$$Q_a = L^T DL = \begin{bmatrix} {L_{11}}^T & {L_{21}}^T & {L_{31}}^T \\ 0 & {L_{22}}^T & {L_{32}}^T \\ 0 & 0 & {L_{33}}^T \end{bmatrix} \begin{bmatrix} D_1 & 0 & 0 \\ 0 & D_2 & 0 \\ 0 & 0 & D_3 \end{bmatrix} \begin{bmatrix} L_{11} & 0 & 0 \\ L_{21} & L_{22} & 0 \\ L_{31} & L_{32} & L_{33} \end{bmatrix} \tag{2.3.12}$$

Here we set P as the identity matrix:

$$P = \begin{bmatrix} 1 & 0 \\ 0 & 1 \end{bmatrix} \tag{2.3.13}$$

$$P_{k,k+1} = \begin{bmatrix} I_{k-1} & & \\ & P & \\ & & I_{n-k-1} \end{bmatrix} \tag{2.3.14}$$

Therefore, we get $P_{k,k+1}^{T} Q_a P_{k,k+1}$ as:

$$\begin{aligned} & {P_{k,k+1}}^{T} Q_a P_{k,k+1} \\ &= \begin{bmatrix} {L_{11}}^{T} & {\overline{L}_{21}}^{T} & {L_{31}}^{T} \\ 0 & {\overline{L}_{22}}^{T} & {\overline{L}_{32}}^{T} \\ 0 & 0 & {L_{33}}^{T} \end{bmatrix} \begin{bmatrix} D_1 & 0 & 0 \\ 0 & \overline{D}_2 & 0 \\ 0 & 0 & D_3 \end{bmatrix} \begin{bmatrix} L_{11} & 0 & 0 \\ \overline{L}_{21} & \overline{L}_{22} & 0 \\ L_{31} & \overline{L}_{32} & L_{33} \end{bmatrix} \end{aligned} \tag{2.3.15}$$

Where

$$D_1 = \mathrm{diag}(d_1, \ldots d_{k-1}) \quad D_3 = \mathrm{diag}(d_{k+2}, \ldots d_n) \quad \overline{D}_2 = \begin{bmatrix} \overline{d}_k & 0 \\ 0 & \overline{d}_{k+1} \end{bmatrix} \tag{2.3.16}$$

$$\overline{d}_{k+1} = d_k + {l^2}_{k+1,k} d_{k+1}, \quad \overline{d}_k = \frac{d_k}{\overline{d}_{k+1}} d_{k+1} \tag{2.3.17}$$

$$\overline{L}_{22} = \begin{bmatrix} 1 & 0 \\ \overline{l}_{k+1,k} & 1 \end{bmatrix}, \quad \overline{l}_{k,k+1} = \frac{d_{k+1} l_{k,k+1}}{\overline{d}_{k+1}} \tag{2.3.18}$$

$$\overline{L}_{21} = \begin{bmatrix} -l_{k+1,k} & 1 \\ \dfrac{d_k}{d_{k+1}} & \overline{l}_{k+1,k} \end{bmatrix} L_{k:k+1,\,1:k-1} \tag{2.3.19}$$

$$\overline{L}_{32} = L_{32} P = [\, L_{k+2:n,k+1} \quad , \quad L_{k+2:n,\,1:k} \,] \tag{2.3.20}$$

2.3.3 Integer Ambiguity Search

After decomposition, we are able to carry out ambiguity searches within the transformed space. Based on the results of these searches, we then convert them back into the ambiguity space in order to find integer answers for the ambiguities. According to section 2.3.2, we get the equations as follows:

$$\hat{z} = Z^T \hat{a} \tag{2.3.21}$$

$$Q_{\hat{z}} = Z^T Q_{\hat{a}} Z \tag{2.3.22}$$

The search space is defined as:

$$(\hat{z} - z)^T Q_2^{-1} (\hat{z} - z) \le X^2 \tag{2.3.23}$$

Following the triangle decomposition of $Q_{\hat{z}}^{-1}$ and subsequent rearrangement, the result is:

$$\sum_{i=1}^{n} \frac{(\hat{z}_{i:I} - z_i)^2}{\sigma_{i:I}^2} \le X^2 \tag{2.3.24}$$

Where $\hat{z}_{i:I}$ is the conditional least square estimator with imposed criteria on $z_1, z_2, z_3, \ldots, z_i$. A good approximation can be obtained using the integer bootstrapping estimator when it comes to determining the size of the search space.

$$X^2 = (\hat{z} - \check{z}_B)^T Q_{\hat{z}}^{-1} (\hat{z} - \check{z}_B) \tag{2.3.25}$$

The sequential intervals are as follows:

$$(\hat{z}_1 - z_1)^2 \leq \sigma^2{}_1 X^2 \tag{2.3.26}$$

$$(\hat{z}_{2:1} - z_2)^2 \leq \sigma^2_{2:1} \left(X^2 - \frac{(\hat{z}_1 - z_1)^2}{\sigma^2{}_1} \right) \tag{2.3.27}$$

The ambiguity with the minimal variance is initially estimated, and this procedure is reiterated until all ambiguities are precisely evaluated using the previously calculated ambiguities.

2.4 Other Correction Methods

2.4.1 Satellite clock and orbit error

Satellite orbital error refers to the inaccuracy that produce by the deviations between the satellite positions given by the satellite ephemeris and their real positions. At present, the International GNSS Service (IGS) is capable of delivering post-processed accurate ephemerides with a precision above 2.5 cm. Therefore, including these ephemerides into GNSS solutions can sufficiently mitigate the influence of satellite orbital errors.

While satellites are supplied with advanced atomic clocks, it is unavoidable that there will be discrepancies between satellites and the standard time of GNSS Systems, known as satellite clock errors. Equally, IGS has the capability to generate accurate clock difference products with a precision exceeding 1 ns, therefore significantly mitigating the influence of satellite clock error.

2.4.2 Relativistic Effect

The state of satellite clocks and receiver clocks, namely their different velocities and gravitational potentials, leads to relative clock errors between them, which is known as the relativistic effect. To mitigate the relativistic effect, the frequency of the satellite clocks is

artificially reduced before launch. However, due to changes in satellite positions and the Earth's gravitational field, the impact of the relativistic effect on satellite clock frequencies is not constant. The satellite position and satellite velocity vectors are respectively referred to as X^s and $\dot{X}^s$, the residual can be eliminated adopting this model as shown below [90].

$$\Delta rel = -\frac{2}{c} \cdot X^s \cdot \dot{X}^s \tag{2.4.1}$$

2.4.3 Phase Wind-up of Satellite

The signals from GNSS satellites incorporate right-hand circular polarization. Rotation of the satellite antenna around its central axis results in a change in the carrier phase measurements. As satellites are required to consistently orient their solar panels towards the sun, the satellite antenna experiences a constant and gradual rotation caused by the satellite's orientation. Observational variations in the carrier phase measurements resulting from this rotation are designated as phase wind-up [91]. Correction of this error can be achieved using the following model:

$$\begin{cases} \delta\phi = sign\left[\overline{k} \cdot \left(\vec{D} \times \vec{D}'\right)\right] \cos^{-1}\left(\dfrac{\vec{D} \cdot \vec{D}'}{|\vec{D}| \cdot \left|\vec{D}'\right|}\right) \\ \vec{D} = \overline{x} - \overline{k} \cdot \left(\overline{k} \cdot \overline{x}\right) - \overline{k} \times \overline{y} \\ \vec{D}' = \overline{x}' - \overline{k} \cdot \left(\overline{k} \cdot \overline{x}\right)'\right) + \overline{k} \times \overline{y}' \\ N = Round\left[\dfrac{\Delta\phi_{previous} - \delta\phi}{2\pi}\right] \\ \Delta\Phi = 2N\pi + \delta\phi \end{cases} \tag{2.4.2}$$

Where $\Delta\Phi$ denotes the phase wind-up correction. $\delta\Phi$ denotes the fractional part of a cycle. D and D' denote two effective dipoles for the receiver the transmitter respectively. N denotes the integer number computed by $\Delta\Phi_{previous}$ which denotes the previous value of phase correction

2.4.4 Receiver Phase Center Offset and Phase Center Variation

Identical to satellite antennas, the receiver antenna phase center offset (PCO) denotes the deviation in which the mean phase center of the reception antenna does not align with the antenna reference point. It is crucial to acknowledge that PCO differs across various frequencies. The receiver antenna phase center variation (PCV) denotes the discrepancy between the current

phase center and the mean phase center of the receiving antenna. Antex files from the International GNSS Service (IGS) include correction information for the primary PCO and PCV across several carrier phase frequencies for different receivers. The PCV data is displayed in a grid structure with high angles ranging from 0 to 90 degrees and azimuth angles ranging from 0 to 360 degrees, with intervals of 5 degrees. For each given direction, the receiver PCV corrections can be acquired by interpolation techniques.

3. Methodology

This chapter presents the Ionosphere-Weighted (IW) UDUC PPP-RTK functional models adopted in this thesis. Then the Adaptive Robust Kalman filter is introduced as the estimator for unknown parameters. Finally, five interpolation techniques for generating ionospheric corrections are shown individually.

3.1 IW UDUC PPP-RTK network model

As parameters in Equation (2.1.9) are linear dependent, the original observation equations cannot be directly adopted in UDUC PPP-RTK. Therefore, based on *S*-basis theory, we need to identify the null space and deal with the issues of rank deficiency. Table 3.1 provides a list of the classes of rank deficiency together with their matching S-basis restrictions. p denotes the pivot receiver and q denotes the pivot satellite. And d_{IF}^{s}, d_{GF}^{s}, $d_{r,IF}$ and $d_{r,GF}$ are given as follows:

$$\begin{cases} d_{IF}^{s} = \dfrac{\mu_2 d_1^s - \mu_1 d_2^s}{\mu_2 - \mu_1}, d_{GF}^{s} = \dfrac{d_2^s - d_1^s}{\mu_2 - \mu_1}, d_{DCB}^{s} = d_2^s - d_1^s \\ d_{r,IF} = \dfrac{\mu_2 d_{r,1} - \mu_1 d_{r,2}}{\mu_2 - \mu_1}, d_{r,GF} = \dfrac{d_{r,2} - d_{r,1}}{\mu_2 - \mu_1}, d_{DCB} = d_{r,2} - d_{r,1} \end{cases} \tag{3.1.1}$$

Table 3.1 Ten forms of rank deficiency, including the associated parameters, size as well as the corresponding S-basis solution for the PPP-RTK network

Type	Involved parameters	Size	S-basis
A	$dt_r(i)\&dt^s(i)$	1	$dt_p(i)$
B	$d_{r,j}\&d_{s,j}$	f	$d_{p,j}$
C	$\delta_{r,j}\&\delta_j^s$	f	$\delta_{p,j}$
D	$dt_{r\neq p}(i)\&d_{r\neq p,j}\&\delta_{r\neq p,j}$	$n-1$	$d_{r\neq p,IF}$
E	$dt^s(i)\&d_j^s\&\delta_j^s$	m	d_{IF}^s
F	$\delta_j^s\&N_{r,j}^s$	$f\cdot m$	$N_{p,j}^s$
G	$\delta_{r\neq p,j}\&N_{r\neq p,j}^s$	$f\cdot(n-1)$	$N_{r\neq p,j}^q$
H	$\tau_r(i)\&dt^s(i)$	1	$\tau_p(i)$
I	$l_r^s(i)\&d_{r\neq p,j}\&\delta_{r\neq p,j}$	$n-1$	$d_{r\neq p,GF}$
J	$l_r^s(i)\&d_j^s\&\delta_j^s$	m	d_{GF}^s

The full-rank UDUC PPP-RTK functional models in network are obtained as Equation (3.1.2) by eliminating the rank deficiencies in Equation (2.1.9) based on the S-basis.

$$\begin{cases} E(\Delta p_{r,j}^{s}(i)) = c\left[\bar{d}t_{r\neq p}(i) - \bar{d}t^{s}(i)\right] + g_1^{s}(i)\cdot\bar{\tau}_{r\neq p}(i) + \mu_j\,\bar{l}_{r}^{s}(i) \\ \qquad\qquad + \bar{d}_{r\neq p,j>2} - \bar{d}_{j>2}^{s} \\ E(\Delta\phi_{r,j}^{s}(i)) = c\left[\bar{d}t_{r\neq p}(i) - \bar{d}t^{s}(i)\right] + g_1^{s}(i)\cdot\bar{\tau}_{r\neq p}(i) - \mu_j\,\bar{l}_{r}^{s}(i) \\ \qquad\qquad + \bar{\delta}_{r\neq p,j} - \bar{\delta}_{j}^{s} + \lambda_j \bar{N}_{r\neq p,j}^{s\neq q} \\ \qquad\qquad 0 = \bar{l}_{p}^{s} - \bar{l}_{r\neq p}^{s} \end{cases} \tag{3.1.2}$$

Where the newly defined parameters denoted by the $\bar{\cdot}$ are defined as Table 3.2.

Table 3.2 Newly defined parameters of the network

Parameter	Formulation
$\overline{dt}^{s}(i)$	$dt^{s}(i) - dt_p(i) + \left[d_{IF}^{s} - d_{p,IF} - g_1^{s}(i)\cdot\tau_p(i)\right]/c$
$\bar{d}_{j>2}^{s}$	$d_j^{s} - d_{IF}^{s} - \mu_j d_{GF}^{s} - d_{p,j} + d_{p,IF} + \mu_j d_{p,GF}$
$\bar{\delta}_{j}^{s}$	$\delta_j^{s} - d_{IF}^{s} + \mu_j d_{GF}^{s} - \delta_{p,j} + d_{p,IF} - \mu_j d_{p,GF} - \lambda_j N_{p,j}^{s}$
$\bar{N}_{r\neq p,j}^{s\neq q}$	$\left(N_{r,j}^{s} - N_{p,j}^{s}\right) - \left(N_{r,j}^{q} - N_{p,j}^{q}\right)$
$\bar{\tau}_{r\neq p}(i)$	$\tau_r(i) - \tau_p(i)$
$\bar{d}_{r\neq p}(i)$	$dt_r(i) - dt_p(i) + (d_{r,IF} - d_{p,IF})/c$
$\bar{d}_{r\neq p,j>2}$	$(d_{r,j} - d_{r,IF} - \mu_j d_{r,GF}) - (d_{p,j} - d_{p,IF} - \mu_j d_{p,GF})$
$\bar{\delta}_{r\neq p,j}$	$\left(\delta_{r,j} - d_{r,IF} + \lambda_j N_{r,j}^{q}\right) - \left(\delta_{p,j} - d_{p,IF} + \lambda_j N_{p,j}^{q}\right)$
$\bar{d}_{r\neq p,DCB}$	$d_{r,DCB} - d_{p,DCB}$
$\bar{l}_{r}^{s}(i)$	$l_r^{s}(i) + d_{p,GF} - d_{GF}^{s}$

As the average distance of Hong Kong reference stations is tens of kilometers, we can add extra constraint to Equation (3.1.2) as:

$$0 = l_p^{s}(i) - l_{r\neq p}^{s}(i), \quad W = S^{-1} \tag{3.1.3}$$

The ionospheric delay's weight matrix in Equation (3.1.3) is represented as S and variance-covariance matrices is represented as W. A further expression for the variance-covariance matrix is:

$$S = c_l^2 \begin{bmatrix} r_{11} & r_{12} & \cdots & r_{1n} \\ r_{21} & r_{22} & \cdots & r_{2n} \\ \vdots & \vdots & \ddots & \vdots \\ r_{n1} & r_{n2} & \cdots & r_{nn} \end{bmatrix} \otimes \begin{bmatrix} c_1^2 & 0 & \cdots & 0 \\ 0 & c_2^2 & \cdots & 0 \\ \vdots & \vdots & \ddots & \vdots \\ 0 & 0 & \cdots & c_m^2 \end{bmatrix} \tag{3.1.4}$$

Where

$$r_{ab} = \exp\left(-\left(\frac{h_{ab}}{h_0}\right)^2\right), c_s^2 = \frac{1}{\sin^2(E^{s})}, \begin{cases} a,b = 1\cdots n \\ s = 1\cdots m \end{cases} \tag{3.1.5}$$

In Equation (3.1.5), c_l represents the priori precision of ionospheric delays. h_{ab} denotes distance of two stations (a and b). h_0 is the empirical distance with the number of 200 kilometers. E^s indicates the elevation angle.

Combining Equation (3.1.3), the I-th rank deficiency in Equation (3.1.2) is eliminated, which can be rewritten as:

$$\begin{cases} E(\Delta p_{r,j}^{s}(i)) = c\left[\, \overline{d}t_{r\neq p}(i) - \overline{d}t^{s}(i)\right] + g_1^{s}(i)\cdot\overline{\tau}_{r\neq p}(i) + \mu_j\,\overline{l}_{r}^{s}(i) \\ \qquad\qquad + \overline{d}_{r\neq p,j>2} - \overline{d}_{j>2}^{s} + \dfrac{\mu_j}{\mu_2-\mu_1}\,\overline{d}_{r\neq p,DCB} \\ E(\Delta\phi_{r,j}^{s}(i)) = c\left[\, \overline{d}_{r\neq p}(i) - \overline{d}t^{s}(i)\right] + g_1^{s}(i)\cdot\overline{\tau}_{r\neq p}(i) - \mu_j\,\overline{l}_{r}^{s}(i) \\ \qquad\qquad + \overline{\delta}_{r\neq p,j} - \overline{\delta}_{j}^{s} + \lambda_j \overline{N}_{r\neq p,j}^{s\neq q} \\ \qquad\qquad 0 = \overline{l}_{p}^{s} - \overline{l}_{r\neq p}^{s} \end{cases} \tag{3.1.6}$$

Where the newly defined parameters are shown as the three bottom columns in Table 3.2.

3.2 IW UDUC PPP-RTK user model

The rank deficiency in user model is similar to network model. Thus, the S-basis to be chosen and the newly defined parameters are nearly the same. And all of the satellite-related parameters in user side are broadcast by the network so that they are regarded as known parameters. Besides, the ionospheric delay of each satellite in user side is generated by the interpolation model using the ionospheric delay in reference stations and the same satellite. Therefore, the user's functional model of IW UDUC PPP-RTK can be derived as:

$$\begin{cases} E\left(\Delta p_{u,j}^{s}(i) + c\,\overline{d}t^{s}(i) + \overline{d}_{j>2}^{s}\right) \\ \quad = c_u^{s}(i)\cdot\Delta x_u(i) + c\hat{d}_u(i) + g_u^{s}(i)\cdot\hat{\tau}_u(i) + \mu_j\hat{l}_u^{s}(i) + \hat{d}_{u,j>2} + \mu_j\hat{d}_{u,GF} \\ E\left(\Delta\phi_{u,j}^{s}(i) + c\,\overline{d}t^{s}(i) + \overline{\delta}_{j}^{s}\right) \\ \quad = c_u^{s}(i)\cdot\Delta x_u(i) + c\hat{d}_u(i) + g_u^{s}(i)\cdot\hat{\tau}_u(i) - \mu_j\hat{l}_u^{s}(i) + \hat{\delta}_{u,j} + \hat{\lambda}_j\widehat{N}_{u,j}^{s\neq q} \\ \overline{l}_{\text{Interpolate}}^{s}(i) = \hat{l}_u(i) \end{cases} \tag{3.2.1}$$

The esteemed representations of the newly defined parameters in user model are listed in Table 3.3.

Table 3.3 Estimable parameters for the PPP-RTK models

Parameter	Fomulation
$\hat{d}_u(i)$	$(dt_u(i) + d_{u,IF}/c) - (dt_p(i) + d_{p,IF}/c)$
$\hat{\tau}_u(i)$	$\tau_u(i) - g_1^s(i)/g_u^s(i) \cdot \tau_p(i)$
$\hat{N}_{u,j}^{s\neq q}$	$\left(N_{u,j}^s - N_{u,j}^q\right) - \left(N_{p,j}^s - N_{p,j}^q\right)$
$\hat{d}_{u,j>2}$	$(d_{u,j} - d_{u,IF} - \mu_j d_{u,GF}) - (d_{p,j} - d_{p,IF} - \mu_j d_{p,GF})$
$\hat{d}_{u,GF}$	$d_{u,GF} - d_{p,GF}$
$\hat{l}_u^s(i)$	$l_u^s(i) - d_{GF}^s + d_{p,GF}$
$\hat{\delta}_{u,j}$	$\left(\delta_{u,j} - d_{u,IF} + \lambda_j N_{u,j}^q\right)$ $- \left(\delta_{p,j} - d_{p,IF} + \lambda_j N_{p,j}^q\right)$

3.3 Adaptive Robust Kalman filter

With the functional models of both network and user proposed, we are able to utilize Adaptive Robust Kalman filter to solve for the unknown parameters. This section takes the PPP model as an example as the process of two techniques is the same. PPP encompasses three categories of observations, among which are pseudorange observations, carrier-phase observations and Doppler observations. Pseudorange observations and carrier-phase observations are crucial to high accuracy positioning, whilst the last one serves as additional measures used to evaluate velocity. Integrating observations in different frequencies can significantly mitigate almost delays caused by atmosphere, facilitating a wide range of applications. Equation (3.3.1) provides the streamlined function model for dual-frequency using Ionosphere-Free (IF) combination [92]:

$$\begin{aligned} P_{IF}^i &= \rho^i + c(dt_r - dt_s^i) + T + \varepsilon_{P_{IF}}^i \\ \Phi_{IF}^i &= \rho^i + c(dt_r - dt_s^i) + T + \lambda_{IF} N_{IF}^i + \varepsilon_{\Phi_{IF}}^i \\ D_{IF}^i &= \dot{\rho}^i + c\left(d\dot{t}_r - d\dot{t}_s^i\right) + \dot{T} + \varepsilon_{D_{IF}}^i \end{aligned} \tag{3.3.1}$$

The superscript i denotes the i_{th} satellite. c denote the speed of light; P_{IF}^i represents the combination of pseudorange P_1 and P_2 that is free of ionospheric delay in two different frequencies f_1 and f_2; Φ_{IF}^i denotes the IF combination of Φ_1 and Φ_2 in the same frequencies. D_{IF}^i is the IF combination of the Doppler D_1 and D_2; ρ denotes the actual distance between satellite and receiver. dt_r and $d\dot{t}_r$ denote the receiver's clock error and clock drift

respectively; $\dot{\rho}$ is the change rate of ρ with time;dt^s denotes the clock error and $d\dot{t}^s$ denotes the clock drift of receivers; T denotes the tropospheric delays and $\dot{T}$ denotes the corresponding change rate; λ_{IF} denotes the IF combination of the carrier-phase wavelengths derived from λ_1 and λ_2; N_{IF}^i denotes the float ambiguity of IF combination; $\varepsilon_{P_{IF}}^i$, $\varepsilon_{\Phi_{IF}}^i$, and $\varepsilon_{D_{IF}}^i$ denote the noise of measurement.

The nonlinear system has following state and observation equations:

$$\begin{aligned} x_k &= f(x_{k-1}) + w_k \\ y_k &= h(x_k) + v_k \end{aligned} \tag{3.3.2}$$

Where x_k denotes the state vector and y_k denotes the observation vector; $f(x)$ represents the dynamic model and $h(x)$ represents the observation model. w_k and v_k represent the white noise vectors in nonlinear system and observations respectively, which are independent.

Utilizing the constant velocity model, the state vector is shown as follows

$$x = (r_r, v_r, cdt_r, Z_r, N_{IF})^T \tag{3.3.3}$$

where $r_r = (x, y, z)$ denotes position of the receiver and $v_r = (v_x, v_y, v_z)$ denotes and velocity in ECEF. Z_r denotes the zenith tropospheric delay. $N_{IF} = (N_{IF}^1, N_{IF}^2, \ldots, N_{IF}^m)$ denotes the IF linear combination of float ambiguities. m represents the quantity of observed satellites.

The vector y is defined as the IF combinations of three kinds of observations:

$$y = (P_{IF}, \Phi_{IF}, D_{IF})^T \tag{3.3.4}$$

where $P_{IF} = (P_{IF}^1, P_{IF}^2, \ldots, P_{IF}^m)$, $\Phi_{IF} = (\Phi_{IF}^1, \Phi_{IF}^2, \ldots, \Phi_{IF}^m)$, and $D_{IF} = (D_{IF}^1, D_{IF}^2, \ldots, D_{IF}^m)$.

The Extended Kalman Filter (EKF) enables the estimation of x for unknown model parameters and its covariance matrix P_x utilizing the observation vector y at a specific epoch t_k as follows:

$$\begin{aligned} \bar{x}_k &= F_{k,k-1}\hat{x}_{k-1} \\ P_{\bar{x}_k} &= F_{k,k-1}P_{\hat{x}_{k-1}}F_{k,k-1}^T + Q_{k,k-1} \\ K_k &= P_{\bar{x}_k}H_k^T\left(H_k P_{\bar{x}_k} H_k^T + R_k\right)^{-1} \\ \hat{x}_k &= \bar{x}_k + K_k(y_k - h(\bar{x}_k)) \\ P_{\hat{x}_k} &= (I - K_k H_k)P_{\bar{x}_k} \end{aligned} \tag{3.3.5}$$

where $\hat{x}_k$ represents the posteriori state vector and $P_{\hat{x}_k}$ represents the covariance matrix respectively at epoch t_k. $F_{k,k-1}$ represents the transformation matrix and $Q_{k,k-1}$ represents the covariance matrix of the process noise w_k between two adjacent epochs t_{k-1}, t_k. $\bar{x}_k$ denotes the predicted state estimation vector. $P_{\bar{x}_k}$ denotes covariance matrix. And H_k denotes coefficient matrix which correlates the actual state space with the observable space and R_k denotes the covariance matrix of observation noise v_k which is assumed to be zero mean Gaussian white noise. K_k denote the Kalman gain to decide whether the result is more inclined to the observed value or the state predicted value.

Regarding the traditional Kalman filter, the state estimation results are highly vulnerable to interference from observation mistakes. Dynamic model mistakes also exert an influence on kinematic positioning. To counteract the impact of both factors, an innovative adaptive robust filter is created by integrating robust estimation with adaptive filtering. Equation (3.3.6) illustrates the recursive solution proposed by the M-M filter theory:

$$\hat{x}_k = \overline{x}_k + \overline{K}_k(y_k - h(\overline{x}_k)) \tag{3.3.6}$$

where $\overline{K}_k$ denotes the Kalman gain in this method:

$$\overline{K}_k = \frac{1}{a_k} P_{\overline{x}_k} H_k^T \left(\frac{1}{a_k} H_k P_{\overline{x}_k} H_k^T + \overline{R}_k \right)^{-1} \tag{3.3.7}$$

where α_k denotes the adaptive factor. $\hat{R}_k$ denotes the covariance matrix of observations noise.

In the presence of significant mistakes in observation data, we can diminish the weights of these erroneous observations by formulating the variance matrix $\bar{R}_k$ computed as:

$$\overline{R}_k = R_k \cdot \overline{P} \tag{3.3.8}$$

For undifferenced model, R_k is a diagonal matrix since each observation is independent of each other. $\bar{P}$ represents the diagonal weight matrix. And P_i is typically computed by Equation (3.3.9) [93]:

$$P_i = \begin{cases} 1 & |\overline{v}_i| \le k_0 \\ \dfrac{|\overline{v}_i|}{k_0}\left(\dfrac{k_1 - k_0}{k_1 - |\overline{v}_i|}\right)^2 & k_0 < |\overline{v}_i| \le k_1 \\ \infty & |\overline{v}_i| > k_1 \end{cases} \tag{3.3.9}$$

where k_0 and k_1 are predefined, typically set as k_0=1.0~2.5, k_1=3.5~8.0. $\bar{v}_i$ denotes the standardized residual calculated as Equation (3.3.10):

$$\overline{v}_i = \frac{v_i}{\sqrt{\hat{\sigma}_0^2 Q_{v_i}}} \tag{3.3.10}$$

where v_i denotes the residual. Q_{v_i} denotes the variance respectively. $\hat{\sigma}_0^2$, denoted as the unit weight variance, is calculated based on the generalized least squares principle using the equation below:

$$\hat{\sigma}_0^2 = \frac{\xi^T Q_\xi^{-1} \xi}{n} \tag{3.3.11}$$

where ξ represents the residual vector of estimation, which can be expressed as $\xi = y_k - h(\bar{x}_k)$. Q_ξ denotes the associated covariance matrix, which can be expressed as $Q_\xi = R_k + H_k P_{\bar{x}_k} H_k^T$. n represents the quantity of observations.

Regarding dynamic carrier-phase measurements, this model is unable to adequately represent the real motion condition. To alleviate the effects of substantial errors in a dynamic model, an adaptive factor is developed to reconcile the dynamic model information with the observations. This factor is defined as:

$$a_k = \begin{cases} 1 & \left|\Delta\tilde{X}_k\right| \le c_0 \\ \dfrac{\left|\Delta\tilde{X}_k\right|}{c_0}\left(\dfrac{c_1 - c_0}{c_1 - \left|\Delta\tilde{X}_k\right|}\right)^2 & c_0 < \left|\Delta\tilde{X}_k\right| \le c_1 \\ \infty & \left|\Delta\tilde{X}_k\right| > c_1 \end{cases} \tag{3.3.12}$$

where c_0 and c_1 are predefined, typically set as c_0=1.0~1.5, c_1=3.0~8.5. $\Delta\tilde{X}_k$ represents the state bias statistic, determined by Equation (3.3.13):

$$\Delta\tilde{X}_k = |\tilde{X}_k - \overline{X}_k| / \sqrt{tr\left(P_{\overline{X}_k}\right)} \tag{3.3.13}$$

where $\tilde{X}_k$ denotes the resilient prediction vector and $\hat{X}_k$ represents anticipated vector. Furthermore, we may select either the predicted residual or the variance component ratio to serve as the statistic.

3.4 Interpolation Models

Upon acquiring the final results of the Kalman filter at the user end, it becomes necessary to categorize the parameters in the state vector. The clock error and hardware bias at the satellite

end will be directly broadcast to the user. While aiming to obtain the user's ionospheric delay correction, it is of vital importance to input the point-to-point ionospheric delay of each satellite and reference station into various ionospheric interpolation models for calculation. This section will present several interpolation models adopted in this thesis.

3.4.1 Inverse Distance Weighted Method

The Inverse Distance Weighted (IDW) technique is an accurate interpolation approach [80]. The method deals with the data by allocating weight to each adjacent point based on their proximity to the predicted location s_0. In the IDW method process, the farther the locations are from s_0, the lower weights the s_0 is received. Moreover, the selection of specific point is entirely contingent upon the user. This is achieved by specifying a radius R around s_0. The IDW method is shown as follows:

$$\hat{z}(s_0) = \frac{\sum_{i=1}^{N} z\,(s_i)\, d_{0i}^{-r}}{\sum_{i=1}^{N} d_{0i}^{-r}} \tag{3.4.1}$$

Where s_0 denotes the interpolated point. N represents the quantity of observations. $z(s_i)$ are observations involved in interpolation. r is the weight decision parameter. d represents the distance.

To provide better understanding of IDW method, the section also introduces the general form of Equation (3.4.1) proposed by Shepard. The fundamental approach is defined as:

$$F(x,y) = \frac{\sum_{k=1}^{N} w_k\,(x,y)\, f_k}{\sum_{k=1}^{N} w_k\,(x,y)} \tag{3.4.2}$$

where the weight w_k is defined as the inverse of Euclidean distance. x and y denote the coordinates. The f_k denotes the observation value of each point involved in interpolation.

Then we define a disk centered at (x_k, y_k) with a radius R, where the weight w_k beyond this disk is set to zero. A common approach proposed by several authors, such as Renka and Brown [94], is encapsulated in the following formula:

$$w_k(x,y) = \left\{ \frac{(R_w - d_k)_+}{R_w d_k} \right\}^2 \tag{3.4.3}$$

And

$$(R_w - d_k)_+ = \begin{cases} R_w - d_k & \text{if } d_k < R_w \\ 0 & \text{if } d_k \geq R_w \end{cases} \tag{3.4.4}$$

Set the conditions that

- The cumulative weights w_k within R_w must satisfy that $\sum w_k = 1$.
- The predictor is formed by linear amalgamation of the data.

The IDW functions are nearly identical to the local kriging interpolator, the only difference is that the covariance structure is not retained. Recently, Fleit proposes the anisotropic IDW method [95]. In this paper, he mentions that the anisotropic IDW method demonstrates better performance and Kriging method also considers anisotropy nature and shows good capability compared with anisotropic IDW method. Therefore, this thesis adopts traditional IDW method for ionospheric correction generations.

3.4.2 Kriging Method

The Kriging method, a linear spatial interpolation technique, is widely used in the field of geostatistics. Recently, its application has expanded into various other fields, including geophysics and the analysis of climate data. Unlike other interpolation techniques like the inverse distance method, Kriging incorporates both spatial and temporal correlations among data points by utilizing the semi-variogram of the sample data [81].

Given the observations $\{Z(s_i)\}_{i=1}^N$, our objective is to estimate the value of $Z(s_0)$ where observations are absent. We aim to identify a suitable estimator $\widehat{Z_0} = \widehat{Z_0}(s_0) = \sum_{i=1}^N w_i Z(s_i)$ that fulfills the specified criteria.

- Unbiasedness. This indicates that $E(Z(s_0)) = E(Z_0)$, which is achieved when $\sum_{i=1}^N w = 1$ and the average value remains unchanged
- Minimum Prediction Variance. It can be classified into various certain conditions based on the mean of the random field $Z(s)$. If this mean is constant but not known throughout the region of interest, the method employed is Ordinary Kriging (OK). If we assume a dominating trend in the data and can represent it with a deterministic function while also

modeling the correlation through random errors, this methodology is referred to as Universal Kriging (UK). If these conditions do not apply, the technique used is referred to as simple kriging.

Consider

$$\begin{aligned}\sigma^2_{\hat{S}_0} &= var\left(Z_0 - \widehat{Z}_0\right)\\ &= var(Z_0) + var\left(\widehat{Z}_0\right) - 2cov\left(Z_0, \widehat{Z}_0\right)\\ &= \sigma^2 + var\left(\sum_{i=1}^{N} w_i Z_i\right) - 2cov\left(Z_0, \sum_{i=1}^{N} w_i Z_i\right)\\ &= \sigma^2 + \sum_{i=1}^{N}\sum_{j=1}^{N} w_i w_j cov(Z_i, Z_j) - 2\sum_{i=1}^{N} w_i cov(Z_i, Z_0)\\ &= \sigma^2 + \sum_{i=1}^{N}\sum_{j=1}^{N} w_i w_j C_{ij} - 2\sum_{i=1}^{N} w_i C_{i0}\end{aligned} \tag{3.4.5}$$

We aim to minimize $var[Z(s_0) - Z(\hat{s}_0)]$ while ensuring that the sum of weights $\sum_{i=1}^{N} w_i = 1$. This optimization is effectively addressed using the method of Lagrange multipliers. To proceed, we construct the Lagrangian L,

$$L = var\left(Z(s_0) - \widehat{Z}(s_0)\right)^2 - 2\lambda\sum_{i=1}^{N}(w_i - 1) \tag{3.4.6}$$

To address this issue, we calculate the partial derivatives of L about the w_i and λ, and set these derivatives equal to zero. From this, we obtain.

$$\begin{bmatrix} w_1 \\ \vdots \\ w_N \\ \lambda \end{bmatrix} = \begin{bmatrix} C_{11} & \cdots & C_{1N} & 1 \\ \vdots & \ddots & \vdots & \vdots \\ C_{1N} & \cdots & C_{NN} & 1 \\ 1 & \cdots & 1 & 0 \end{bmatrix}^{-1} \begin{bmatrix} C_{10} \\ \vdots \\ C_{N0} \\ 1 \end{bmatrix} \tag{3.4.7}$$

Equation (3.4.7), also known as the Kriging model, is utilized to determine the weights. These weights can be divided into two parts, the interpolation nodes with interpolation nodes and interpolated nodes with interpolation nodes. And the former's solutions for these weights are derived by their covariance calculated as:

$$C_{ij} = C(s_i, s_j) = Cov(Z_i, Z_j) \quad \forall i,j \tag{3.4.8}$$

Where the covariance matrix can be written as:

$$C = \begin{bmatrix} C_{11} & \cdots & C_{1N} \\ \vdots & \ddots & \vdots \\ C_{1N} & \cdots & C_{NN} \end{bmatrix} \tag{3.4.9}$$

And for the latter's solutions for these weights are calculated as:

$$C_{i0} = C(s_i, s_0) = Cov(Z(s_i), Z(s_0)) \quad \forall i. \tag{3.4.10}$$

Where the covariance matrix can be written as:

$$c = [C_{10} \;\; C_{20} \;\; \cdots \;\; C_{N0}]^{\mathrm{T}} \tag{3.4.11}$$

Equation (3.4.7) above becomes

$$\begin{bmatrix} w \\ \lambda \end{bmatrix} = \begin{bmatrix} C & 1 \\ 1^{\mathrm{T}} & 0 \end{bmatrix}^{-1} \begin{bmatrix} c \\ 1 \end{bmatrix} \tag{3.4.12}$$

Here w denotes the weights as $1 \times N$ matrix. 1 denotes the vector whose elements are all 1. The spatial correlation between each point is calculated by the semi-variogram functions:

$$\begin{aligned} \gamma(h) &= \frac{1}{2} var(Z(s_i) - Z(s_j)) \\ &= \frac{1}{2} \{var(Z(s_i)) + var(Z(s_j)) \\ &\qquad - 2cov(Z(s_i), Z(s_j))\} \\ &= C(0) + C(h), \end{aligned} \tag{3.4.13}$$

where $C(0)$ and $C(h)$ denote the variance and the covariance respectively. Both the variogram and the covariance are able to perform the same function because they both carry the same information.

For example, the spatial correlation function $C(h)$ can be calculated by:

$$C(h) = \frac{\sigma^2}{2^{v-1}\Gamma(v)} (\kappa|h|)^{v} K_v(\kappa|h|) \tag{3.4.14}$$

Where $h = \|s_i - s_j\| \in R^+$ denotes the Euclidean spatial distance between each point. K_V denotes the modified Bessel function of the second kind, where the order $V > 0$ quantifies the smoothness of the procedure. κ represents the scaling parameter associated with the distance of decorrelation. And $C(h)$ is derived as follows:

$$f(\omega) = \phi(\alpha^2 + \omega^2)^{-(v+1/2)} \quad v > 0, \phi > 0, \alpha > 0 \tag{3.4.15}$$

3.4.3 Least Square Collocation

Attributing to the trend-signal-noise model and least-squares prediction theory, we can generate ionospheric correction by the Least-Squares Collocation (LSC) approach [82]. The ionospheric delay, as the trend term, is hypothesized as the average ionospheric delay value of all stations at the same satellite within measurement cone. This assumption is deemed reasonable when it is low and normal ionospheric activity day.

Therefore, let's explore the segmented linear system of equations associated with the vector $\hat{\tilde{\imath}}$ of ionospheric delays, where $\hat{\tilde{\imath}} = [\hat{\tilde{\imath}}_1^T, \ldots, \hat{\tilde{\imath}}_n^T]^{\mathrm{T}}$, $\hat{\tilde{\imath}}_r = [\hat{\tilde{\imath}}_1^1, \ldots, \hat{\tilde{\imath}}_r^m]^{\mathrm{T}}$. $\bar{l} = [\bar{l}^1, \ldots, \bar{l}^m]^{\mathrm{T}}$ is the spatial mean ionospheric delay of each satellite. The ionospheric delay of user is defined as the vector $\tilde{l}_{net \to u} = [\tilde{l}_{net \to u}^1, \ldots, \tilde{l}_{net \to u}^m]^{\mathrm{T}}$. Here we get Equation (3.4.16) as follows:

$$E\left(\begin{bmatrix} \hat{\tilde{l}} \\ \tilde{l}_{\mathrm{net} \to u} \end{bmatrix}\right) = \begin{bmatrix} e_n \otimes I_m & C_n \otimes e_m \\ I_m & 0_{m \times (n-1)} \end{bmatrix} \begin{bmatrix} \bar{l} \\ \tilde{d}_{p'r,\mathrm{GF}} \end{bmatrix} \tag{3.4.16}$$

Where m represents the quantities of satellites and n represents the quantities of network stations. e_n represents an n-vector whose elements are all 1. I_n represents a unit n-th matrix. $\tilde{l}_{p'r,GF} = [\tilde{l}_{p'2,GF}, \ldots, \tilde{l}_{p'n,GF}]^{\mathrm{T}}$. C_n denotes an n-th order identity matrix which excludes the first column. $\otimes$ is the Kronecker product. In this thesis, the first receiver is selected as the based receiver.

The Variance-Covariance (V-C) matrix of LSC corrections incorporates the errors from measurements and noises inherent in the signals. Given that the PPP-RTK corrections are supplied perpetually by the server, we can obtain the ionospheric delay estimations from the network which achieve significant accuracy over time, rendering their associated V-C matrix negligible. Consequently, the remaining V-C matrix is the only one to focus. To address the spatial correlation in the ionosphere, the Gaussian function is utilized, known for its reducing correlation effect and ensuring the positive definiteness [96]:

$$h_{ij} = c_l^2 \exp\left(-\left(\frac{l_{ij}}{l_0}\right)^2\right) \tag{3.4.17}$$

Here h_{ij} denotes the correlation function for two receivers. The variance c_l^2 represents the value of the covariance function at zero. l_{ij} denotes the geographical distance of the two receivers. l_0 denotes a predetermined inter-station distance with the aim of describing spatial correlation. exp (·) represents the natural exponential function. Consequently, the V-C matrix is delineated by:

$$D\left(\begin{bmatrix} \hat{\tilde{l}} \\ \tilde{l}_{\mathrm{net} \to u} \end{bmatrix}\right) = \begin{bmatrix} H_{ij} & H_{iu} \\ H_{iu}^{\mathrm{T}} & H_{uu} \end{bmatrix} \otimes I_m, i, j = 1, \ldots, n \tag{3.4.18}$$

Where D and H respectively represent the dispersion operator and the correlation matrix computed using the aforementioned equation.

Consequently, according to BLUP [97][98], the ionospheric delays are calculated by:

$$\hat{\tilde{l}}_{\text{net}\to u} = \hat{\bar{l}} + [(H_{iu}^{\mathrm{T}} H_{ij}^{-1}) \otimes I_m]\left(\hat{\tilde{l}} - [e_n \otimes I_m]\,\hat{\bar{l}} - [C_n \otimes e_m]\hat{\tilde{d}}_{p'r,\mathrm{GF}}\right) \quad (3.4.19)$$

Where the optimal linear unbiased estimators of $\bar{l}$ and $\bar{\tilde{d}}_{p'r,GF}$ are derived from the equation as:

$$\begin{bmatrix} (e_n^{\mathrm{T}} H_{ij}^{-1} e_n) \otimes I_m & (e_n^{\mathrm{T}} H_{ij}^{-1} C_n) \otimes e_m \\ (C_n^{\mathrm{T}} H_{ij}^{-1} e_n) \otimes e_m^{\mathrm{T}} & (C_n^{\mathrm{T}} H_{ij}^{-1} C_n) \cdot m \end{bmatrix} \begin{bmatrix} \hat{\bar{l}} \\ \hat{\tilde{d}}_{p'r,\mathrm{GF}} \end{bmatrix} = \begin{bmatrix} (e_n^{\mathrm{T}} H_{ij}^{-1}) \otimes I_m \\ (C_n^{\mathrm{T}} H_{ij}^{-1}) \otimes e_m^{\mathrm{T}} \end{bmatrix} \hat{\tilde{l}} \quad (3.4.20)$$

And we have the expectation of Equation (3.4.19) as follows:

$$E\left(\hat{\tilde{l}}^{\,s}_{net\to u}\right) = \tilde{l}^{\,s}_{net\to u} = l_u^s - \tilde{d}^{\,s}_{,\mathrm{GF}}, \quad \text{with} \quad \tilde{d}^{\,s}_{,\mathrm{GF}} = d^{\,s}_{,\mathrm{GF}} - d_{p',\mathrm{GF}} \quad (3.4.21)$$

3.4.4 Planar Fitting

Owing to the spatial correlation of the ionospheric delay, it is possible to calculate the ionospheric delay in user and provide a precise error bound for an Ionospheric Grid Point (IGP) based on observations from N Ionospheric Power Points (IPPs) within a specific radius surrounding that IGP. We employ a local Cartesian coordinate system with its origin situated at the IGP. The x-axis of this frame is oriented towards the East at the IGP and the y-axis is oriented towards the North. The ionospheric delay of each IPP in this grid is computed by [83]:

$$I_{v,IPP}(x,y) = \hat{a}_0 + \hat{a}_1 \cdot x + \hat{a}_2 \cdot y \quad (3.4.22)$$

Where $I_{v,IPP}\,(x,y)$ denotes the vertical estimated ionospheric delay, where x denotes the longitudinal distance and y denotes the latitudinal distance between different IPPs. $I_{v,IPP}$ with corresponding variances $\sigma^2_{v,IPP}$ can be defined as:

$$I_{v,IPP} = \begin{bmatrix} I_{v,IPP_1} \\ I_{v,IPP_2} \\ \vdots \\ I_{v,IPP_N} \end{bmatrix} \quad (3.4.23)$$

$$\sigma_{v,IPP}^2 = \begin{bmatrix} \sigma_{v,IPP_1}^2 \\ \sigma_{v,IPP_2}^2 \\ \vdots \\ \sigma_{v,IPP_N}^2 \end{bmatrix} \tag{3.4.24}$$

Here the σ_{v,IPP_i}^2 represents the boundary variance relating to frequency for the i_{th} IPP that characterizes noise uncertainty. The observation matrix is defined by

$$G^{\mathrm{T}} = \begin{bmatrix} 1 & d_{IPP_1,IGP} \cdot \hat{E} & d_{IPP_1,IGP} \cdot \hat{N} \\ 1 & d_{IPP_2,IGP} \cdot \hat{E} & d_{IPP_2,IGP} \cdot \hat{N} \\ \vdots & \vdots & \vdots \\ 1 & d_{IPP_n,IGP} \cdot \hat{E} & d_{IPP_n,IGP} \cdot \hat{N} \end{bmatrix} \tag{3.4.25}$$

where $d_{IPP_i,IGP}$ (i = 1, 2, …, n) is the distance between IPP$_i$ and the IGP. $\hat{E}$ represents the east direction in ECEF, while $\hat{N}$ denotes the north direction.

The weighting matrix of IPPs is written as:

$$\begin{aligned} W^{-1} = diag\Big(&\sigma_{I_{v,IPP_1}}^2 + \sigma_{decorr}^2, \cdots \\ &\sigma_{I_{v,IPP_{N-1}}^2}^2 + \sigma_{decorr}^2, \sigma_{I_{v,IPP_N}^2}^2 + \sigma_{decorr}^2 \Big) \end{aligned} \tag{3.4.26}$$

where σ_{decorr} denotes the uncertainty, which is set to 35cm. The planar coefficients can be determined as:

$$[\hat{a}_0 \quad \hat{a}_1 \quad \hat{a}_2] = \left((G \cdot W \cdot G^T)^{-1} \cdot G \cdot W \cdot I_{v,IPP}\right)^{\mathrm{T}} \tag{3.4.27}$$

Therefore, we can calculate the ionospheric delay and the error as:

$$\hat{I}_{v,IGP} = \hat{a}_0 \tag{3.4.28}$$

$$\hat{\sigma}_{\hat{I}_{\mathrm{I,IGP}}^2} = (G \cdot W \cdot G^{\mathrm{T}})^{-1} \tag{3.4.29}$$

The planar model can be assessed using the estimated values obtained from filtering to generate predictions for each IPP.

$$\hat{I}_{v,IPP} = \begin{bmatrix} 1 \\ d_{IPP,IGP} \cdot \hat{E} \\ d_{IPP,IGP} \cdot \hat{N} \end{bmatrix}^{\mathrm{T}} \cdot \begin{bmatrix} \hat{a}_0 \\ \hat{a}_1 \\ \hat{a}_2 \end{bmatrix} \tag{3.4.30}$$

4. Experiments and Results

4.1 Software Platform

This thesis utilizes a MATLAB-based software named PPPH as the basic platform. The software is open source and has a comprehensive manual, which highly supports secondary development. The flowchart of the original PPPH is depicted in Figure 4.1. This software has the capability to deal with multi-GNSS PPP data in the post-processing mode. Furthermore, it utilizes a dual-frequency ionosphere-free model. Utilizing the original PPPH, we modify this software and convert the functional model into the model as illustrated in chapter 3. The previous model exclusively receives single station observation data and computes the position of a single receiver once. With the modifications, our algorithm is capable of simultaneously resolving various station data as the network side. What's more, we add the segment of interpolation models and user's position calculation into the software. All subsequent experimental verifications in this thesis are also carried out based on the modified PPPH.

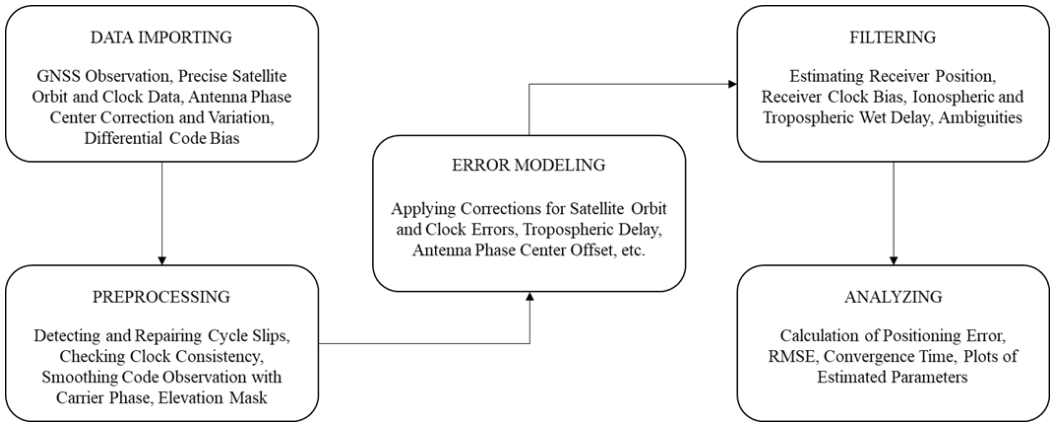

Figure 4.1 Operation flowchart of PPPH with its components

4.2 Experiments

4.2.1 Processing Strategy

The network of IW UDUC PPP-RTK in this thesis consists of 16 chosen Hong Kong reference stations to generate the corrections. The observation data of these reference stations is acquired from the Geodetic Survey of Hong Kong in 30s intervals. The PCOs and PCVs for

satellite and receiver are corrected adopting the ANTEX file based on the IGS absolute antenna model. The satellite orbit errors and clock errors are mitigated with SP3 and CLK files respectively provided by IGS and MGEX analysis centers. Since all receivers are equivalent, the first receiver is chosen as the based receiver. For each station, the based satellite is the one with the highest elevation angle. Other data processing strategies used in this thesis are shown as Table 4.1

Table 4.1 Data processing strategy

Items	**Strategies**
Frequency	GPS L1&L2
Estimator	Robust Adaptive Kalman filter
Weighting strategy	Based on the elevation angle
Priori accuracy	Pseudorange measurements as 0.3 m; Carrier phase measurements as 0.3 cm
Tropospheric delays	A priori value generated by UNB3m; Estimated as random-walk noise 0.001 m; The ZHD is mitigated using Saastamoinen model
Ionospheric delays	Server: defined as white noise to calculate; User: defined as white noise or constrained by various interpolation models from server
Elevation cut-off angles	8 degrees;
Cycle slip identification	MW combination
Ambiguity	Server: defined as float constants to solve; User: LAMBDA method to fix

4.2.2 Selection of Date

The geomagnetic three-hourly Kp index was created by J. Bartels in 1949. It is calculated by the standardized K index (Ks) from magnetic observations. It is constructed to quantify solar particle radiation through its magnetic effects and is now regarded as a proxy for the energy influx from the solar wind to Earth. Consequently, this article employs this indicator to assess ionospheric activity. The value is supplied by GFZ German Research Centre for Geosciences as eight intervals daily. To better compare the interpolation methods, other influencing factors need to be eliminated as much as possible. Therefore, this research chooses July in 2021, a month characterized by low and moderate ionospheric activity, for the comparison of ionospheric interpolation methods and the accuracy assessment of the accompanying PPP-RTK. To facilitate a more effective comparison of daily ionospheric activity, we aggregate the eight Kp values for each day, with the results illustrated in Figure 4.2. And Table 4.2 shows the detailed Kp values of each day in July.

Figure 4.2 indicates that the Kp value peaks on the 14th day at 19, signifying maximum ionospheric activity. The Kp value on the 25th is 3.6, the lowest in the month, signifying optimal ionospheric stability; thus, we select the data from these two days for analysis. Furthermore, we select the 18th day with a Kp value of 6.7, indicative of moderate ionospheric activity, to analyze the data concurrently.

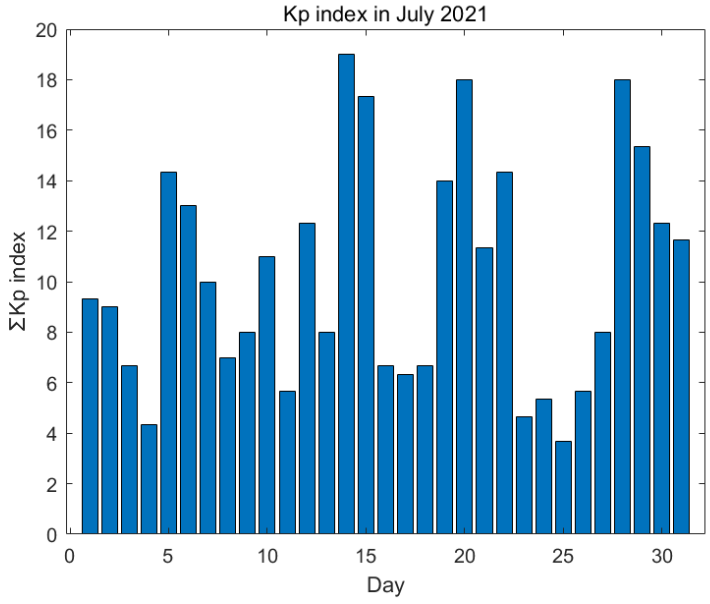

Figure 4.2 Kp index of each day in July 2021

Table 4.2 Detailed Kp in July

Day	Interval numbers with Kp exceeding 2	Max Kp
14	3	4.333
20	1	2.333
22	1	3.333
28	2	3.667
Other days	0	N/A

4.2.3 Identification of parameters for LSC

Section 3.4.3 indicates the presence of an indeterminate parameter l_0 in the LSC technique. The value of this parameter influences the computation of the variance-covariance matrix for ionospheric interpolation, hence impacting the accuracy of the ionospheric delay estimation at the final interpolated location. Consequently, ascertaining the predetermined distance in Hong Kong is crucial to this topic, and the value of this parameter must be specified beforehand.

To minimize the interpolation error caused by the active ionosphere during the calculation of the preset distance, we select July 25th, a day characterized by ionospheric stability, for estimation. We selected the HKPC station as the interpolated point and the remaining 15 reference stations as interpolation points to compute the root mean square of the estimated value. The data were collected from 10:52:30 to 20:00:00 on July 25th, 2021 (Local time, UTC + 8).

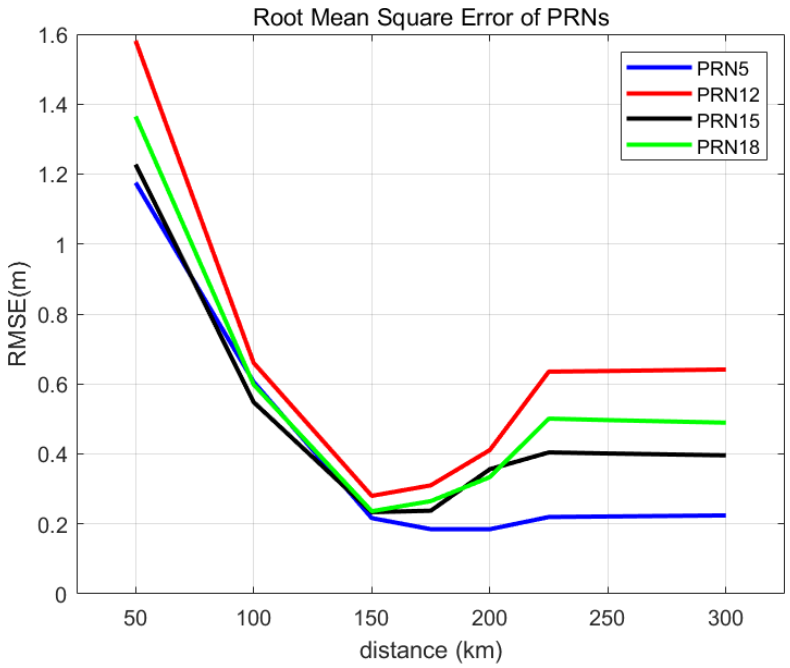

Figure 4.3 Root Mean Square Error of several PRNs

As demonstrated in Figure 4.3, when l_0 is below 150 km, the root mean square of each satellite diminishes swiftly with increasing value. When l_0 exceeds 200 km and is less than 225 km, the root mean square value typically rises with the increase of l_0. When l_0 exceeds 225 km, the root mean square tends to flatten.

To simplify the calculation, we assume the minimal RMSE value when l_0 is 175 km. Then we interpolate all satellites, and calculate the average RMSE of each satellite, as seen in Table 4.3. Table 4.3 further confirms the principle of RMSE variation with distance and verifies that in Hong Kong, the interpolation precision is maximized when the specified distance in LSC technique is 175 km. Thus, in the ensuing comparisons on interpolation techniques, the specified distance for the LSC approach is set at 175 km.

Table 4.3 Average RMSE of all satellites in each value of distance

Distance (km)	Average RMSE (m)
50	1.542
100	0.805
150	0.376
175	0.354
200	0.368
225	0.403
250	0.403
300	0.403

4.3 Comparisons of Interpolation Methods

The ionospheric delays for each station and each date are initially computed adopting the UDUC PPP-RTK network model as true values. We select two stations—HKPC and HKSS—as interpolated stations due to their locations inside the geographical borders of the Hong Kong reference station network and their relative distance from one another. The ionospheric delays are interpolated utilizing five techniques: the Inverse Distance Weighting (IDW) method, the Least Squares Collocation (LSC) method, the Ordinary Kriging (OK) method, the Universal Kriging (UK) method, and the Planar Fitting (PF) method. Finally, the residuals of the ionospheric delays between the interpolated and true values using both techniques as well as the Root Mean Square Error (RMSE) and standard deviation (STD) are computed.

The temporal range for interpolation is from 10:00 to 20:00, encompassing a total of 1,200 epochs. The data from the initial 105 epochs are utilized for variogram modeling in the Kriging method, with interpolation commencing at 10:52:30.

4.3.1 Interpolation accuracy of Network I

The geographical distribution of Network I is illustrated in Figure 4.4, with the Hong Kong HKPC station serving as the interpolated point and the other stations functioning as reference stations.

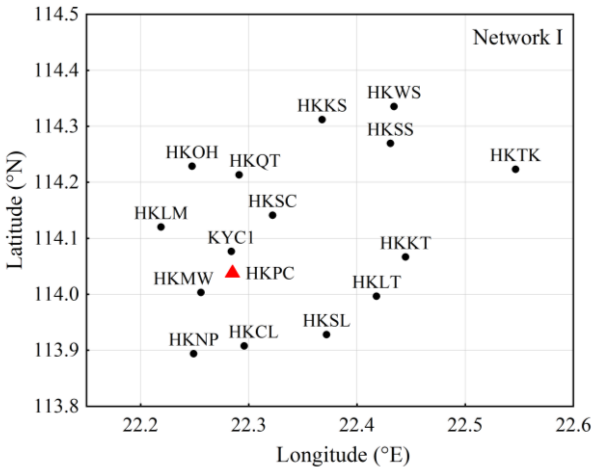

Figure 4.4 Geographical distribution of Network I

Utilizing the aforementioned interpolation approaches, we obtain the ionosphere estimation value for each satellite at the HKPC station. By comparing it with the actual value of each satellite, we can calculate the estimation error for each satellite. First, we select July 25th, a day characterized by stable ionospheric activity. The interpolation errors for three sample satellites are depicted in Figure 4.5.

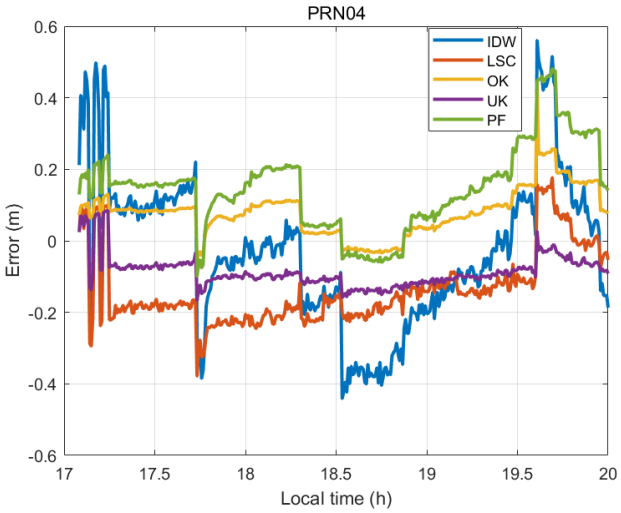

(a)

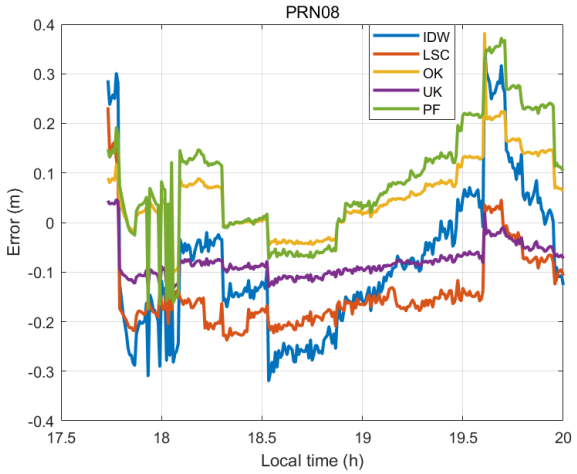

(b)

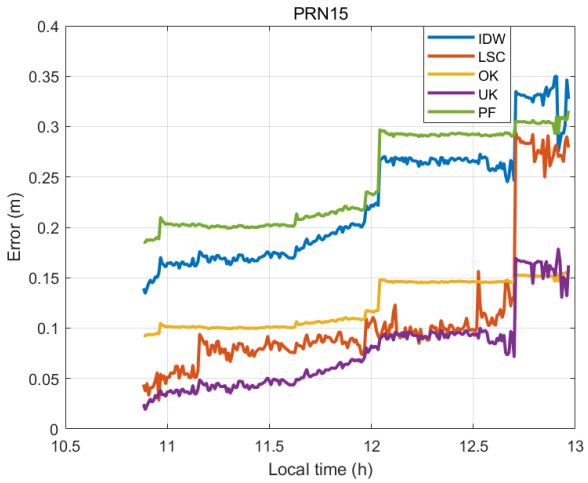

(c)

Figure 4.5 Errors of ionospheric delay on July 25th

(a) PRN04 (b) PRN08 (c) PRN15

The aforementioned figure demonstrate that both the OK method and the UK method exhibit commendable stability while the UK method shows superior stability with the error range consistently remaining within 0.2m. The PF, LSC, and IDW method exhibit significant swings in errors, with particular periods experiencing values that can surpass 0.4m. Subsequently, utilizing the acquired error data, we can calculate the RMSE and standard deviation, as seen in Figure 4.6 and Figure 4.7.

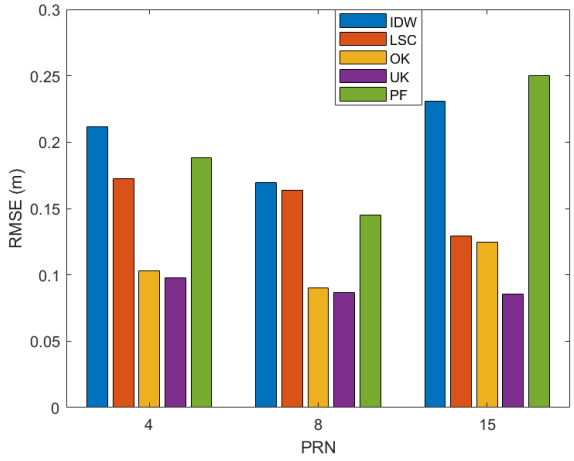

Figure 4.6 RMSE of HKPC on July 25th

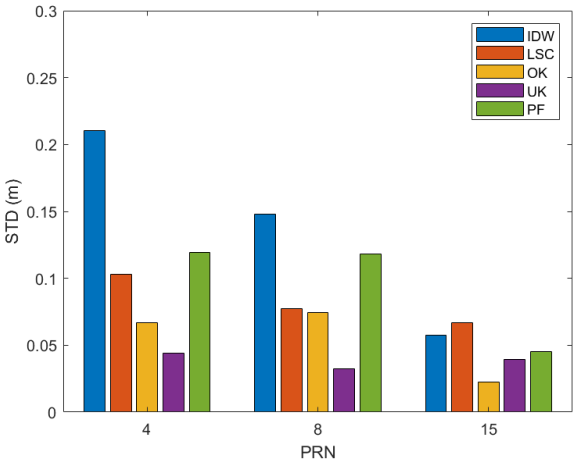

Figure 4.7 STD of HKPC on July 25th

Figure 4.6 and 4.7 illustrate that the RMSE of both the IDW and PF methods is the highest, accompanied by a comparatively significant standard deviation. The RMSE and STD of the LSC method rank second, however the RMSE remains at 0.15m. The RMSE and standard deviation of the UK method and the OK method are comparatively lower, with the UK method exhibiting the lowest values. Consequently, it is determined that the UK approach exhibits optimal performance in HKPC station during quiet day of the ionosphere.

Then the interpolation results at the HKPC station on July 18, a typical day of ionospheric activity, is computed, which are shown as Figure 4.8.

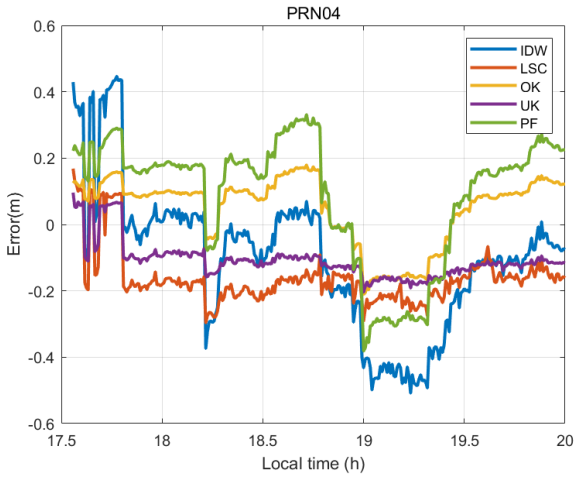

(a)

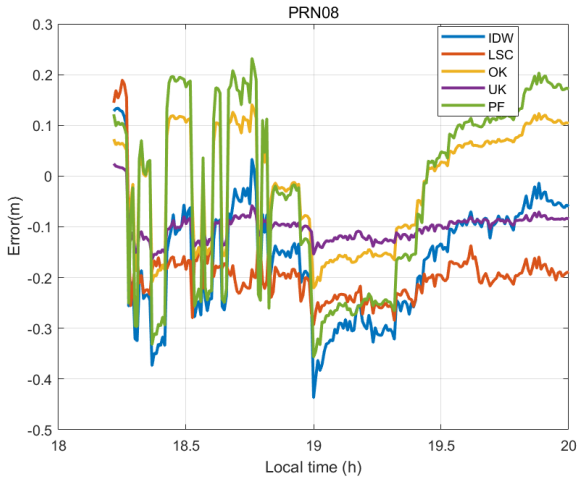

(b)

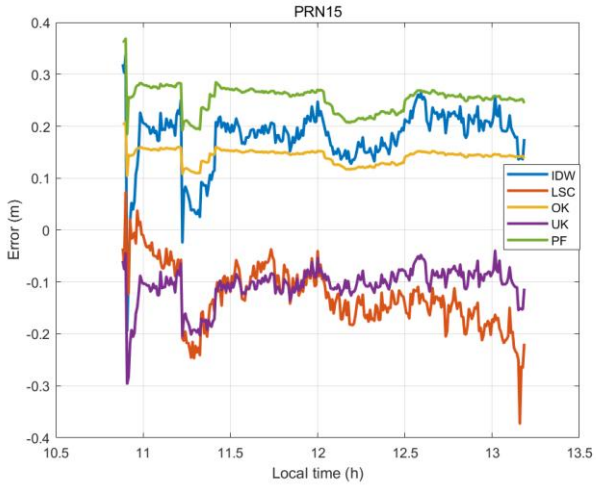

(c)

Figure 4.8 Errors of ionospheric delay on July 18th

(a) PRN04 (b) PRN08 (c) PRN15

Figure 4.8 illustrates that, in comparison to the interpolation results from July 25, the five interpolation methods have heightened the degree of fluctuation on the 18th. The UK approach exhibits minimal volatility, with values generally remaining below 0.2m. While the OK technique exhibits significant variability in the interpolation error of PRN08, the findings for the other two satellites demonstrate more consistent fluctuations, with the overall value remaining below 0.2m. The range of fluctuation and values of the other three methods remain substantial, with peak values reaching 0.4m.

Subsequently, utilizing the acquired error data, we can also calculate the RMSE and STD of July 18th, as seen in Figure 4.9 and 4.10.

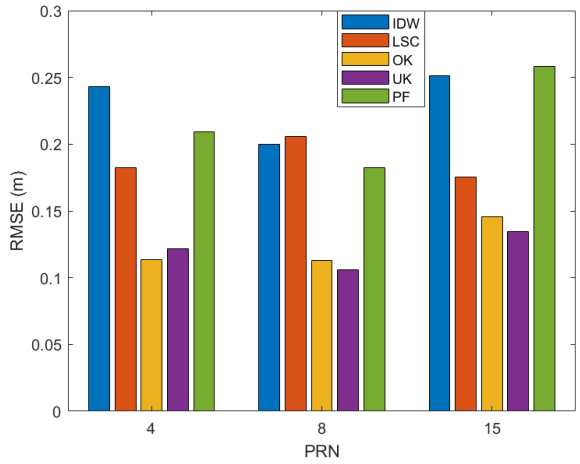

Figure 4.9 RMSE of HKPC on July 18th

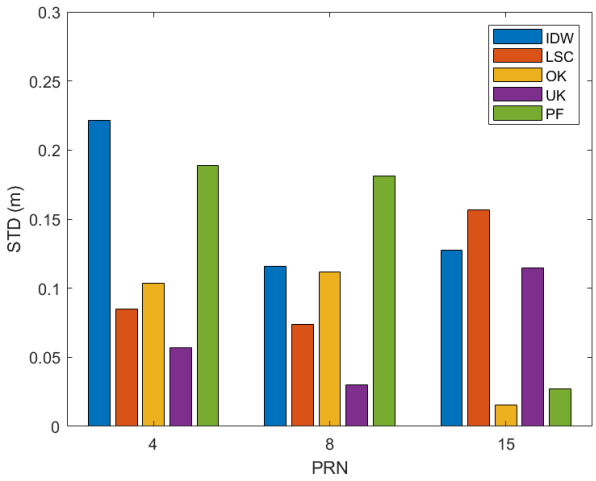

Figure 4.10 STD of HKPC on July 18th

In comparison to the results from the 25th, the RMSE and STD of the five interpolation methods have all increased. This results from heightened ionospheric activity. Furthermore,

among these five methods, the RMSE of the UK method is the least, the OK method is somewhat greater, while the RMSE of the remaining three methods remains higher. Regarding standard deviation, the OK method and the UK method exhibit the lowest values, while the remaining three methods demonstrate higher values. The detailed data indicate that the UK technique exhibits superior performance, aligning with the findings from the 25th.

Finally, the data for July 14 with the peak ionospheric activity, is calculated as illustrated in Figure 4.11.

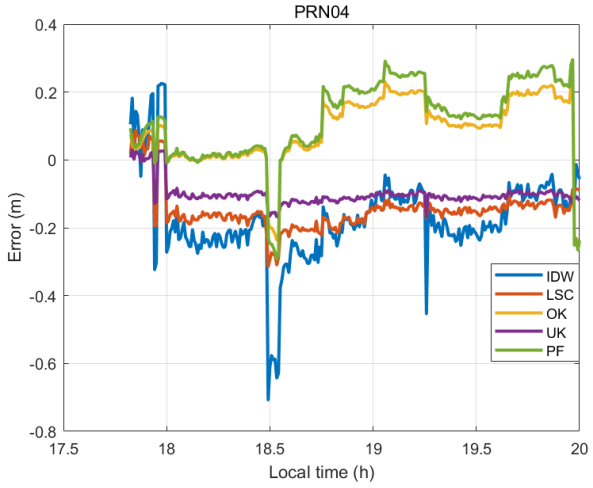

(a)

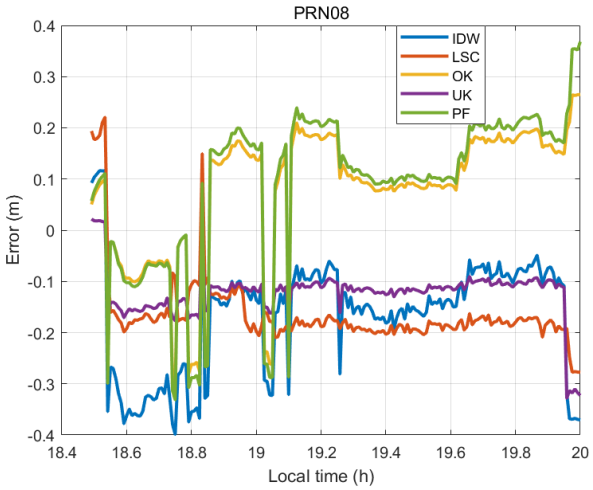

(b)

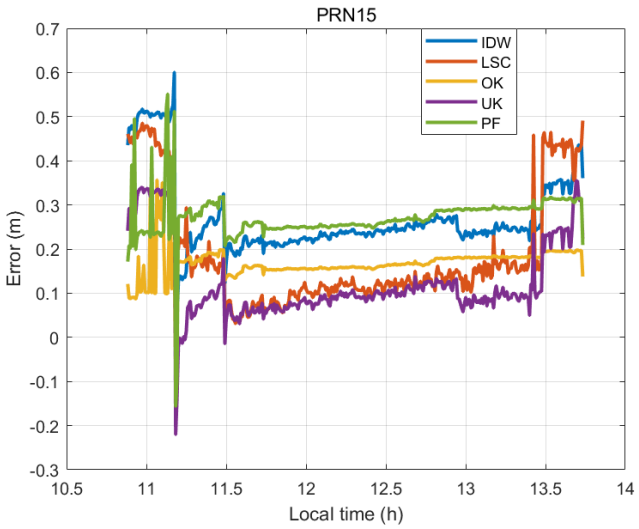

(c)

Figure 4.11 Errors of ionospheric delay on July 14th

(a) PRN04 (b) PRN08 (c) PRN15

Figure 4.11 indicates that the interpolation results from the three satellites have surpassed those from the 18th in numerical value, attributable to heightened ionospheric activity. Among the five approaches, the UK method exhibits the least error and the most consistent variation. The OK approach has a broader range of variability and error escalation, whereas the errors associated with the other three methods remain significant, accompanied by an extensive range of variation. The RMSE and STD of the five interpolation methods are then computed. The results are presented in Figure 4.12 and 4.13.

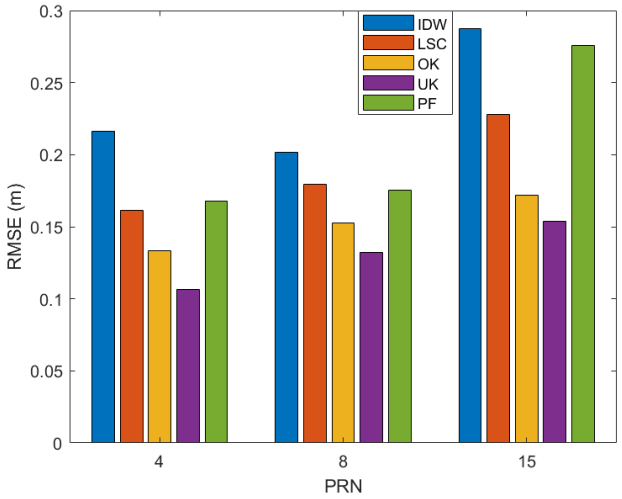

Figure 4.12 RMSE of HKPC on July 14th

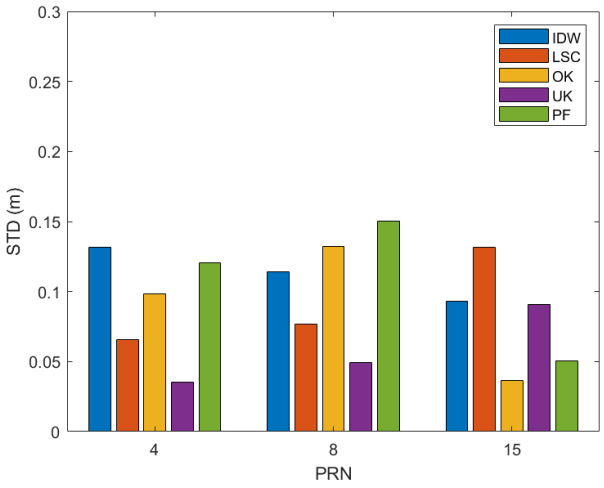

Figure 4.13 STD of HKPC on July 14th

Figure 4.12 and 4.13 suggest that the RMSE of the three satellites, particularly PRN08, have further escalated relative to the results from the 18th. Regarding STD, while the variation is not apparent in comparison to the 18th, it remains elevated relative to the 25th. The UK method continues to have the lowest RMSE and STD among them. By amalgamating the interpolation results from three days, it is evident that the efficacy of various interpolation methods across different satellites exhibits a degree of consistency, with the UK method typically demonstrating superior performance. Consequently, in network I, the UK method is the most appropriate interpolation method.

4.3.2 Interpolation accuracy of Network II

The distribution of Network II is depicted in Figure 4.14, with HKSS station acting as the interpolated point and the remaining stations serving as reference stations. Similar to Network I, we utilize the ionospheric delay generated from the network and five interpolation methods to generate the ionospheric delay for each satellite in HKSS station. The dates also coincide with those in Network I: July 25, a quiet day; July 18, a day with ordinary ionospheric activity; and July 14, a disturbed day. The interpolation results on the 25th are shown in Figure 4.15.

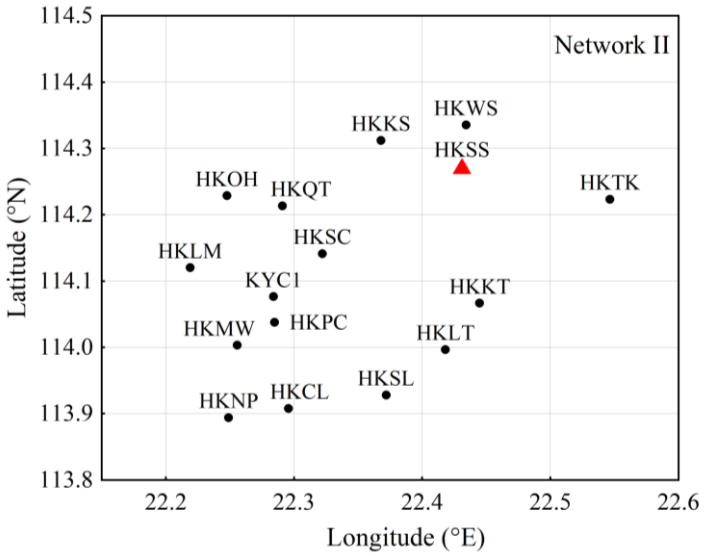

Figure 4.14 Geographical distribution of Network II

Figure 4.15 depicts that, among the three satellites, the UK technique exhibits the least error in the five methods, with a fluctuation range maintained within ±0.2m. The error and fluctuation range of the OK method in the middle part of the period are identical to those of the UK method; however, the error is greater in the first and last thirty minutes. The errors of the LSC method and the PF method are greater, but remain below 0.4m, with more pronounced fluctuations. The error of the IDW method is the largest, with a maximum value of 0.5m. Moreover, except for the PRN15 satellite, the variances of the remaining two satellites remain significant.

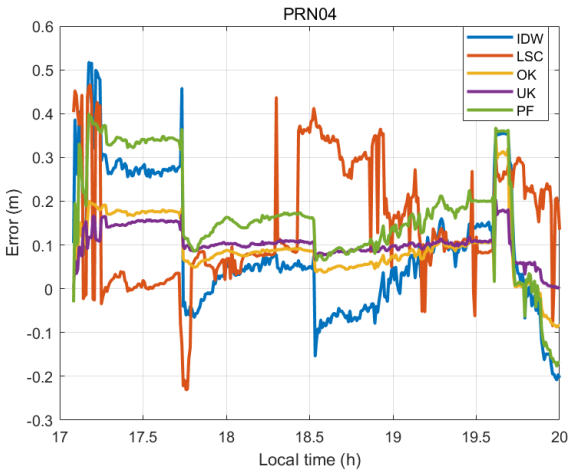

(a)

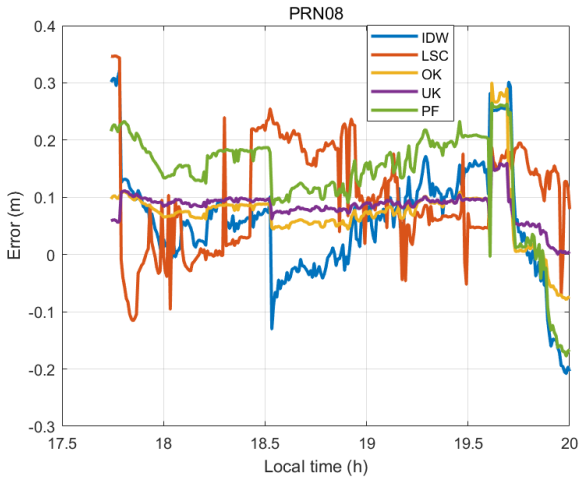

(b)

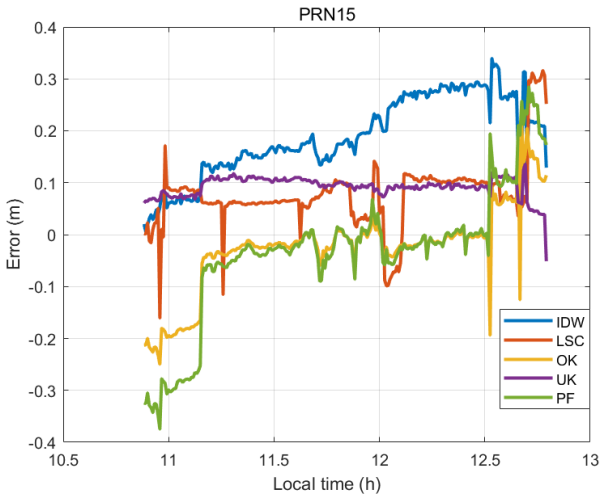

(c)

Figure 4.15 Errors of ionospheric delay on July 25th

(a) PRN04 (b) PRN08 (c) PRN15

The RMSE and STD of the five interpolation methods are then computed as presented in Figure 4.16 and 4.17. Figure x shows that the RMSE of both the UK method and the OK method is approximately 0.09m in the three satellites, with the STD remaining below 0.1m. The performance of the UK technique is superior to the OK technique marginally. The RMSE and STD of the LSC method for the PRN15 satellite are 0.09m and 0.06m, respectively, although the corresponding values for the other two satellites are comparatively larger. The RMSE and STD of the IDW method and the PF method are elevated with respect to the other three methods. Consequently, we can ascertain that the UK method exhibits superior performance in the interpolation outcomes for the HKSS station on July 25th.

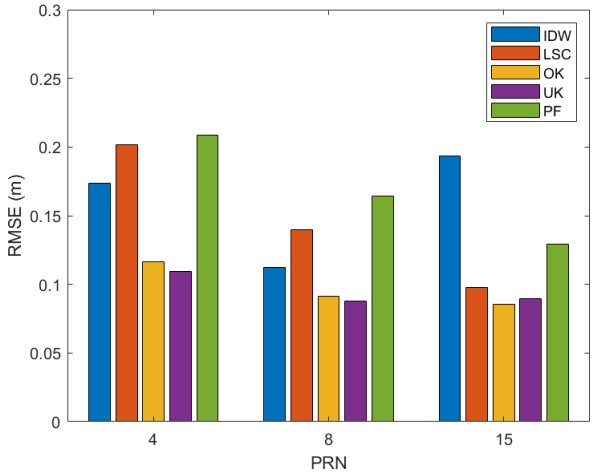

Figure 4.16 RMSE of interpolation methods in HKSS on July 25th

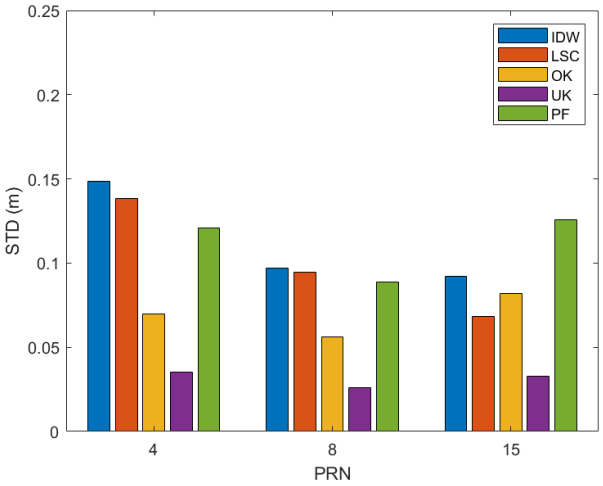

Figure 4.17 STD of interpolation methods in HKSS on July 25th

Then the interpolation results at the HKSS station on July 18, a typical day of ionospheric activity, is computed, which are shown as Figure 4.18.

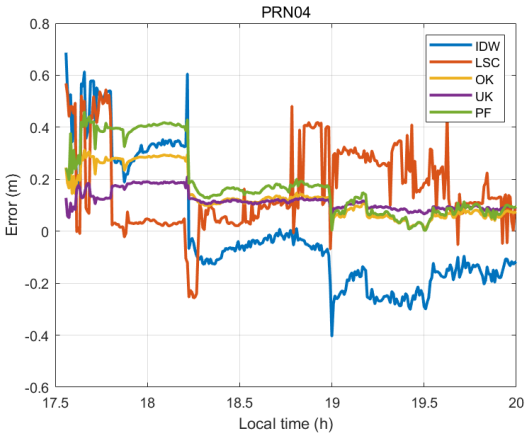

(a)

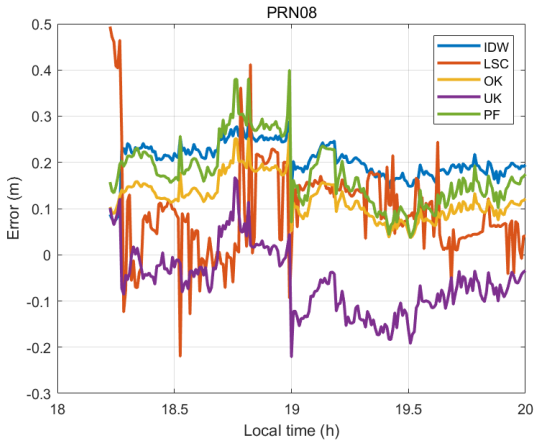

(b)

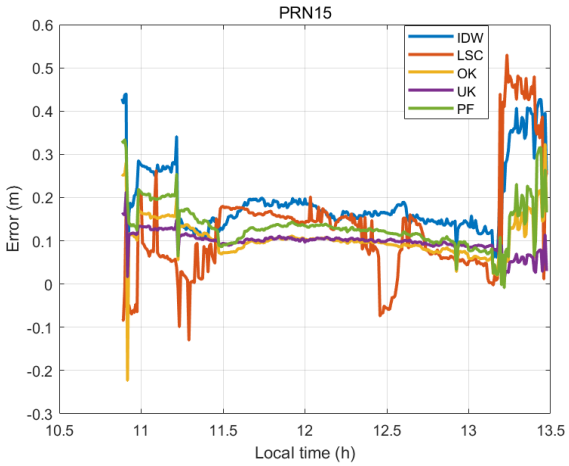

(c)

Figure 4.18 Errors of ionospheric delay on July 18th

(a) PRN04 (b) PRN08 (c) PRN15

By comparing Figure 4.15 and Figure 4.18, it is obvious that the interpolation errors of the five methods on the 18th increase relative to those on the 25th, with a greater range of fluctuation. The UK method exhibits very steady results for the PRN04 and PRN15 satellites, while the error fluctuation range is greater for PRN08; however, the interpolation errors for all three satellites remain below 0.2m. The performance of the OK method in PRN04 and PRN08 is comparable to that of the UK approach; however, it exhibits significant swings in PRN15. The remaining three approaches show significant errors and substantial fluctuation. The RMSE and STD of the five interpolation methods are then computed as presented in Figure 4.19 and 4.20.

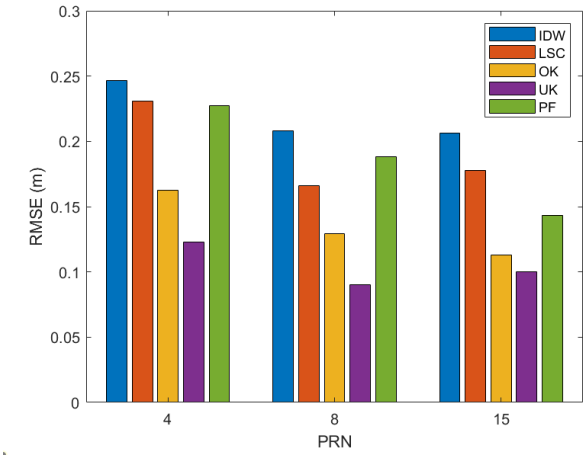

Figure 4.19 RMSE of interpolation methods in HKSS on July 18th

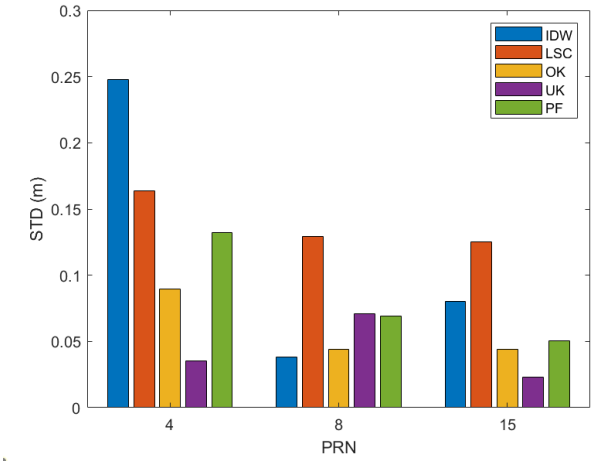

Figure 4.20 STD of interpolation methods in HKSS on July 18th

Figure 4.19 and 4.20 depict that the RMSE of the UK method is the lowest among the five methods, averaging approximately 0.1m. With the exception of the PRN08 satellite, which has a standard deviation of 0.07m, the STD of all other satellites are below 0.05m. The OK method ranks second to the UK approach in terms of RMSE and STD. The values of RMSE and STD in the other three methods are higher, indicating their performances are subpar compared to the OK method and the UK method. Finally, the data for July 14 with the peak ionospheric activity, is calculated as illustrated in Figure 4.21.

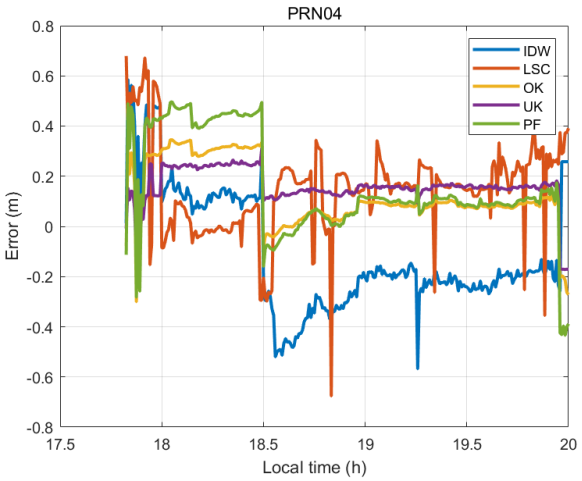

(a)

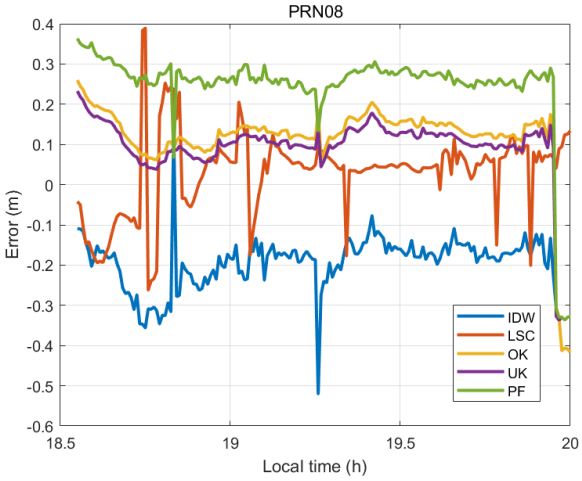

(b)

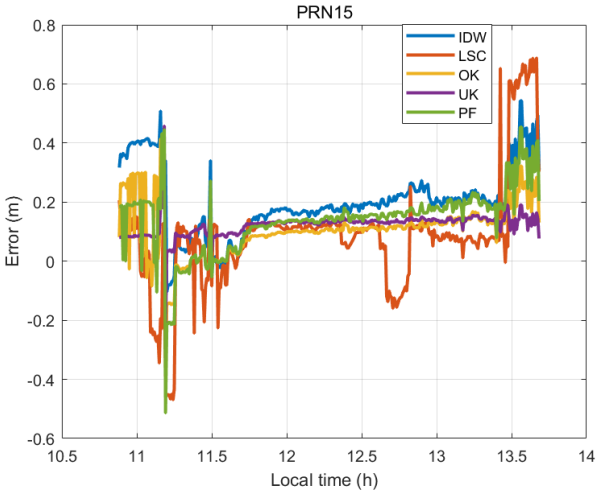

(c)

Figure 4.21 Errors of ionospheric delay on July 14th

(a) PRN04 (b) PRN08 (c) PRN15

Figure 4.21 demonstrates that the interpolation error has increased relative to the result on the 18th, attributable to more intense ionospheric activity. Among the five interpolation methods, the UK method has superior performance on all three satellites, exhibiting both the lowest value of error and the most confined range. The errors of the OK approach are modest, but generally exceeds that of the UK method. And the OK method exhibits a broader range of shifts in the PRN15 satellite. The interpolation errors of the remaining three methods remain large, and the range of fluctuation is more pronounced than the results obtained on the 18th. The RMSE and STD of the five interpolation methods are then computed as presented in Figure 4.22 and 4.23.

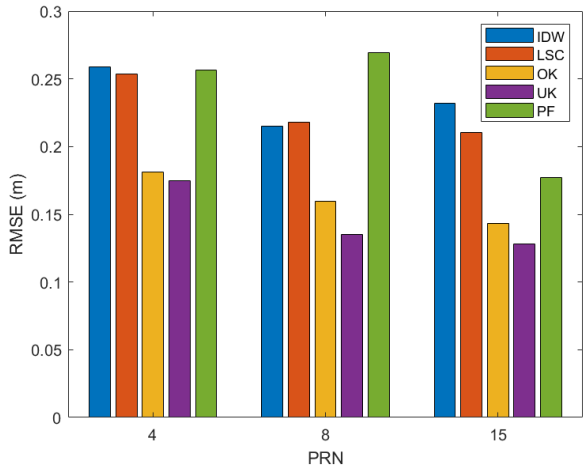

Figure 4.22 RMSE of interpolation methods in HKSS on July 14th

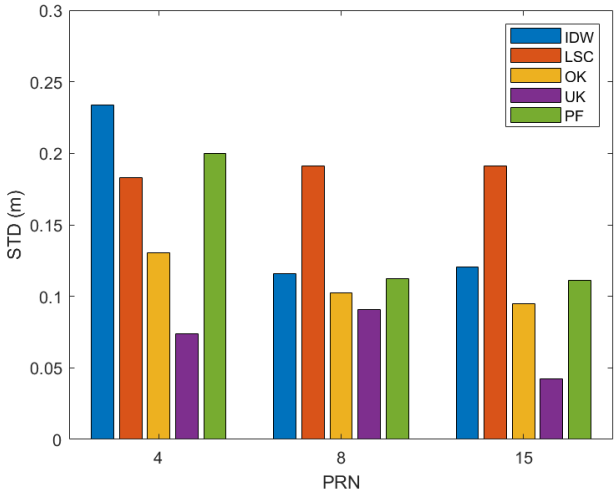

Figure 4.23 STD of interpolation methods in HKSS on July 14th

Figure 4.22 and 4.23 further reinforces our findings. Despite the increase in the RMSE and STD of five methods compared to the data from the 18th, the UK method remains the most

reliable, with an RMSE of approximately 0.15m and a STD of around 0.07. The OK method has inferior performance compared to the UK method, however remains quantitatively comparable to it.

The performance of the other three approaches significantly diverges from that of the UK method. Aggregating the findings from the three days, the UK technique exhibits the least inaccuracy across different levels of ionospheric activity. When integrated with the findings from Network I, it is evident that in regions like Hong Kong, characterized by low latitude and minimal reference station distance, the UK method emerges as the best appropriate interpolation method.

4.4 Comparison of Positioning Performance

This section evaluates and examines the positioning performance of UDUC PPP-RTK employing various ionospheric interpolation methods. Utilizing five interpolation approaches, we can get the estimated ionospheric delay for each satellite at the interpolated position, which will serve as priori restrictions on the ionospheric delay at the user end. Subsequently, employing the satellite phase delay, satellite clock error, and hardware bias supplied from the network, ambiguity resolution and coordinate resolution are executed on the user end. As we select several stations within the reference station network as the user end, the coordinates of the user are known, allowing for an analysis of the positioning result accuracy.

In this experiment, we choose HKPC and HKSS stations as the user ends, while the remaining reference stations compose the server ends. The experimental dates are July 14th, 18th, and 25th, corresponding to the high ionospheric activity day, the normal ionospheric activity day, and the low ionospheric activity day, respectively. Upon obtaining the positioning results of users adopting the processing strategy outlined in section 4.2.1, we compute the RMSE and STD of north, east and vertical directions before and after ambiguity resolution. Additionally, we also record and compare the time-to-first-fix (TTFF) of each method.

4.4.1 Positioning performances in Network I

We firstly evaluate the positioning accuracy of the UDUC PPP-RTK method in Network I. The geographical distribution of this network is illustrated in Figure 4.4, with the HKPC station serving as the user end and the other stations serving as the server end. The experimental date is the 25th, and the test period corresponds to that in section 4.3. The results are presented in Table 4.4.

Table 4.4 demonstrates that the UDUC PPP-RTK method, employing five interpolation techniques, achieves decimeter-level accuracy before the ambiguity resolution and achieves millimeter-level accuracy after the ambiguity resolution. Of the five approaches, the UK method exhibits the highest positioning accuracy, following by the OK method and the LSC method, while the IDW method and the PF method have the lowest accuracy. Moreover, the UK method and the OK method exhibit the lowest STD, indicating that their positioning results are the most stable. The STDs of the remaining three approaches are rather substantial. The TTFF for all five approaches ranges from 7s to 9s, with the UK method being the quickest at 7.12s.

Table 4.4 Positioning accuracy of UDUC PPP-RTK for Network I on July 25th

Method	RMSE (m)			Fixed RMSE (cm)			STD (m)	Fixed STD (cm)	Mean TTFF (s)
	N	E	U	N	E	U			
IDW	0.26	0.41	0.77	0.25	0.20	0.82	0.37	0.26	7.42
LSC	0.16	0.21	0.60	0.24	0.12	0.65	0.32	0.17	8.21
OK	0.12	0.15	0.43	0.27	0.18	0.63	0.28	0.11	7.29
UK	0.13	0.17	0.36	0.21	0.14	0.61	0.23	0.10	7.12
PF	0.14	0.19	0.49	0.27	0.17	0.74	0.20	0.36	8.88

Subsequently, we compute the positioning results on the 18th, as illustrated in Table 4.5. In comparison to the results on the 25th, the positioning accuracy of the five approaches has diminished. The accuracy before the ambiguity resolution has decreased to the meter level, whereas the accuracy after the resolution is at the millimeter to centimeter level. Moreover, the

TTFF of the five approaches has experienced a modest increase. Among the five approaches, the UK method exhibits the highest positioning accuracy, followed by the OK method, which maintains an accuracy at the millimeter level. The accuracy of the remaining three approaches has diminished to the centimeter level. Regarding STD, the UK method and the OK method exhibit the fewest values, indicating significantly greater stability. Additionally, the TTFF of the UK method remains the lowest.

Table 4.5 Positioning accuracy of UDUC PPP-RTK for Network I on July 18th

Method	RMSE (m)			Fixed RMSE (cm)			STD (m)	Fixed STD (cm)	Mean TTFF (s)
	N	E	U	N	E	U			
IDW	0.41	0.61	1.26	0.37	0.40	1.37	0.33	0.40	8.57
LSC	0.34	0.63	1.29	0.34	0.54	1.24	0.26	0.36	8.79
OK	0.46	0.54	1.12	0.31	0.36	0.84	0.28	0.15	7.94
UK	0.37	0.46	1.09	0.25	0.30	0.69	0.21	0.14	7.53
PF	0.58	0.85	1.67	0.48	0.51	1.28	0.30	0.45	9.14

Finally, we computed the results on the 14th, as shown in Table 4.6. Compared with the data from the 18th, the positioning accuracy of the five ways has further diminished, particularly the accuracy after ambiguity resolution, which has declined to the centimeter level. The TTFF of the five methods has also grown further. Among the five ways, the UK method exhibits the best positioning accuracy and the least increment. The accuracy of the OK approach is comparable to that of the UK method while the accuracy of the remaining three approaches has diminished markedly, particularly in the vertical direction. In terms of STD, the UK method and the OK method remains the least; nonetheless, it has increased markedly compared to the 18th, which also can be observed in the other three ways. Besides, the OK approach exhibits the lowest TTFF among the five methods at 8.93s. All other ways are similar to the OK technique, except for the IDW method, which is 10.17s.

Table 4.6 Positioning accuracy of UDUC PPP-RTK for Network I on July 14th

Method	RMSE (m)			Fixed RMSE (cm)			STD (m)	Fixed STD (cm)	Mean TTFF (s)
	N	E	U	N	E	U			
IDW	0.63	0.83	1.47	0.84	0.97	2.98	0.46	0.54	10.17
LSC	0.60	0.68	1.35	0.73	0.91	2.26	0.48	0.43	9.02
OK	0.48	0.59	1.26	0.67	0.81	1.51	0.39	0.36	8.93
UK	0.41	0.50	1.29	0.58	0.51	1.30	0.26	0.27	9.24
PF	0.68	0.89	1.73	0.81	0.82	1.92	0.47	0.60	9.33

By aggregating the results from the three days, it can be concluded that the UK method exhibits superior positioning performance across different levels of ionospheric activity, the OK method demonstrates marginally inferior positioning performance compared to the UK method, while the positioning performance of the other methods are relatively worse.

4.4.2 Positioning performances in Network II

Then we evaluate the positioning accuracy of the UDUC PPP-RTK method in Network II. The geographical distribution of this network is illustrated in Figure 4.15, with the HKSS station serving as the user end and the other stations serving as the server end. All other experimental conditions are identical to those of Network I.

Table 4.7 indicates that the accuracy of the five techniques is at the decimeter level before ambiguity resolution and can achieve millimeter-level after ambiguity resolution, which is comparable to Network I. The UK approach exhibits the highest positioning accuracy, with the accuracy of the other four methods similar to that of the UK method. The UK method and the OK method have the lowest standard deviation, approximately 0.19 cm, whereas the standard deviations of the other methods are greater. Regarding TTFF, all five methods range from seven to eight seconds, with the UK approach exhibiting the lowest value of 7.14s.

Table 4.7 Positioning accuracy of UDUC PPP-RTK for Network II on July 25th

Method	RMSE (m)			Fixed RMSE (cm)			STD (m)	Fixed STD (cm)	Mean TTFF (s)
	N	E	U	N	E	U			
IDW	0.11	0.18	0.39	0.26	0.23	0.86	0.32	0.54	7.64
LSC	0.29	0.26	0.48	0.25	0.18	0.82	0.31	0.57	7.16
OK	0.16	0.14	0.26	0.21	0.13	0.74	0.24	0.18	7.16
UK	0.07	0.13	0.21	0.21	0.10	0.63	0.17	0.19	7.14
PF	0.13	0.19	0.29	0.27	0.19	0.96	0.21	0.30	7.38

Then, we calculated the results on the 18th, as shown in Table 4.8. In comparison to the results on 25th, the positioning accuracy of the five methods has decreased. Although the accuracy before the ambiguity resolution is still maintained at the decimeter level, the accuracy after resolution has dropped to the centimeter level in the vertical direction. In addition, the STD and TTFF of the five methods have also increased. Among the five methods, the UK method still has the highest positioning accuracy, maintaining millimeter-level accuracy in three directions. The accuracy of the other four methods has diminished relatively significantly, particularly in the vertical direction. In terms of standard deviation, the UK method still has the lowest STD of 0.27cm, but it has increased compared to the 25th. The TTFF of the five approaches has marginally risen, however all remain below eight seconds. The UK technique is the smallest, measuring 7.42s.

Table 4.8 Positioning accuracy of UDUC PPP-RTK for Network II on July 18th

Method	RMSE (m)			Fixed RMSE (cm)			STD (m)	Fixed STD (cm)	Mean TTFF (s)
	N	E	U	N	E	U			
IDW	0.19	0.24	0.49	0.57	0.46	1.65	0.42	0.84	7.98
LSC	0.30	0.46	0.61	0.44	0.58	1.38	0.39	0.67	7.67
OK	0.20	0.16	0.38	0.38	0.52	1.02	0.34	0.31	7.58
UK	0.19	0.12	0.32	0.35	0.47	0.89	0.26	0.27	7.42
PF	0.32	0.25	0.54	0.51	0.54	1.41	0.28	0.36	7.72

At last, we calculate the results on the 14th, as shown in Table 4.9 In comparison to the results from the 18th, the positioning accuracy of the five approaches diminished before and after ambiguity, achieving meter-level and centimeter-level accuracy, respectively. The TTFF of the five approaches also increase further. Of the five ways, the UK method exhibits the highest accuracy, with millimeter-level accuracy in the north and east directions, as well as superior accuracy in the vertical direction. The accuracy of the OK technique is comparable to that of the UK method, whereas the accuracy of the other three methods has markedly declined, mirroring the trend observed in Network I. As for STD, the standard deviation of the UK method and the OK method remains the smallest, yet it has increased considerably compared to the 18th, which is also observed in the other three methods. The OK and UK approaches have the lowest TTFF among the five methods, approximately 7.9s, while the remaining methods exceed 8s.

Table 4.9 Positioning accuracy of UDUC PPP-RTK for Network II on July 14th

Method	RMSE (m)			Fixed RMSE (cm)			STD (m)	Fixed STD (cm)	Mean TTFF (s)
	N	E	U	N	E	U			
IDW	0.54	0.84	1.39	1.47	1.56	3.14	0.94	1.35	8.11
LSC	0.57	0.76	1.22	1.35	1.44	2.57	0.75	1.22	8.42
OK	0.36	0.45	0.98	0.76	0.81	1.61	0.69	0.74	7.92
UK	0.18	0.33	0.78	0.59	0.68	1.48	0.58	0.61	7.91
PF	0.42	0.55	1.18	1.24	1.35	2.94	0.87	1.13	8.01

According to the results from the three-day evaluation, the UK technique exhibits superior positioning performance in Network II, with the highest accuracy and a more rapid resolution. This is identical to the conclusion drawn in Network I. The performance of the OK method is inferior to that of the UK method, while reasonably similar. And the positioning performances of other ways are unsatisfactory.

4.5 Discussions

Firstly, it is obvious that almost all RMSE of interpolation error in the beginning and the end of observation time increase. This is because the elevation angle of satellite is the smallest during these periods. Thus, the ionospheric delay will be extremely affected. To mitigate this, we can increase the elevation cut-off angles to decrease the fluctuations in ionospheric errors.

Secondly, as this thesis focuses on Hong Kong, the problems of oversampling and ill-conditioned matrices cannot be avoided. But there are solutions to mitigate the impact of these issues. By using multi-constellation observation data and assigning higher weights to satellites with higher elevation angles, we can acquire more valuable data as much as possible. Therefore, the issues of spatial underrepresentation can be resolved.

Lastly, the results from sections 4.3 and 4.4 indicate that in Hong Kong, characterized by relatively short inter-station distance and low latitude, the UK method is the most appropriate interpolation technique for UDUC PPP-RTK. This approach exhibits high interpolation accuracy and superior positioning performance, while also sustaining effective performance

during high ionospheric active days. This is because the kriging interpolation method comprehensively considers the spatial correlation and the geographical distribution of the reference stations in computations. And the UK method exhibits superior accuracy compared to the OK method due to its effective error modeling capabilities. While the IDW method and the PF method disregard these factors. The IDW approach and the PF method presume that all points possess analogous features, disregard spatial autocorrelation, and exhibit sensitivity to noise. As the LSC method considers spatial correlation, the directly employed exponential function model is not generally applicable, and the predetermined distance setting significantly influences the interpolation accuracy.

5. Summary

This study examines various ionospheric interpolation techniques, including the Inverse Distance Weighting (IDW) method, the Least Squares Collocation (LSC) method, the Ordinary Kriging (OK) method, the Universal Kriging (UK) method, and the Planar Fitting (PF) method, based on Ionosphere-Weighted UDUC PPP-RTK model. The objective is to identify the most appropriate interpolation method for Hong Kong and promote the performances of PPP-RTK. This thesis utilizes the open-source software PPPH for extended development as the platform and analyzes the interpolation accuracy and positioning performance using data from 16 stations in Hong Kong region. By conducting studies on days with different levels of ionospheric activity, we conclude that the UK method has the best interpolation accuracy and positioning performance, making it the optimal interpolation method for PPP-RTK positioning in Hong Kong.

Nonetheless, this thesis has certain limitations. The findings presented in this research cannot be universally applicable to all locations due to differences in latitudes and reference station networks. When conducting PPP-RTK positioning in different regions, it is necessary to reevaluate the interpolation method in that area to guarantee the accuracy of PPP-RTK positioning. Furthermore, the other interpolation methods require further research and comparison. Our subsequent efforts will focus on these limits and enhance the performance of UDUC PPP-RTK.

References

[1] Kouba J, Heroux P (2001) Precise point positioning using IGS orbit and clock products. GPS Solution 5(2):12–28.

[2] Zumberge J, Heflin M, Jefferson D, Watkins M, Webb FH (1997) Precise point positioning for the efficient and robust analysis of GPS data from large networks. J Geophys Res Solid Earth 102(B3):5005–5017.

[3] Dow JM, Neilan RE, Rizos C (2009) The international GNSS service in a changing landscape of global navigation satellite systems. J Geod 83(3–4):191–198.

[4] Øvstedal, O., Ofstad, A., Haustveit, K. and Kristiansen, O. (2002). An empirical comparison between absolute satellite positioning methods and differential methods in a maritime environment. In Proceedings of ION GPS 2002, Portland, OR. Institute of Navigation.

[5] Wang, S., B. Li, H. Ge, and Z. Zhang. 2020. "Algorithm and assessment of ambiguity-fixed PPP with BeiDou observations and regional network augmentation." J. Surv. Eng. 146 (2): 04020009.

[6] Boisits, J.; Glaner, M.; Weber, R. Regiomontan: A regional high precision ionosphere delay model and its application in Precise Point Positioning. Sensors 2020, 20, 2845.

[7] Banville, S., Geng, J., Loyer, S., Schaer, S., Springer, T., & Strasser, S. (2020). On the interoperability of IGS products for precise point positioning with ambiguity resolution. Journal of Geodesy, 94(1), 10.

[8] Collins, P. (2008). Isolating and estimating undifferenced GPS integer ambiguities. In Proceedings of the 2008 national technical meeting of the institute of navigation, San Diego, CA, USA (pp. 720–732).

[9] Laurichesse, D., Mercier, F., Berthias, J. P., Broca, P., & Cerri, L. (2009). Integer ambiguity resolution on undifferenced GPS phase measurements and its application to PPP and satellite precise orbit determination. Navigation - Journal of the Institute of Navigation, 56(2), 135–149.

[10] Teunissen, P. J. G. (1995). The least squares ambiguity decorrelation adjustment: A method for fast GPS integer estimation. Journal of Geodesy, 70, 65–82.

[11] Teunissen, P. J. G., & Khodabandeh, A. (2015). Review and principles of PPP-RTK methods. Journal of Geodesy, 89(3), 217–240.

[12] Ge et al., 2008. Resolution of GPS carrier-phase ambiguities in Precise Point Positioning (PPP) with daily observations. Journal of. Geodesy, 82 (2008), pp. 389-399.

[13] P. Collins, S. Bisnath, L. Francois, P. Héroux. Undifferenced GPS ambiguity resolution using the decoupled clock model and ambiguity datum fixing. Journal of Navigation, 57 (2) (2010), pp. 123-135.

[14] Laurichesse, D., F. Mercier, J.P. Berthias, Bijac, J (2008). Real Time Zero-difference Ambiguities Blocking and Absolute RTK, Proceedings of the ION/NTM 2008, 28-30.

[15] J. Geng, F.N. Teferle, C. Shi, X. Meng, A.H. Dodson, J (2009). Liu Ambiguity resolution in Precise Point Positioning with Hourly data. GPS Solution, 13 (4), pp. 263-270.

[16] Geng J, Wen Q, Zhang Q, Li G, Zhang K (2022) GNSS observable-specific phase biases for all-frequency PPP ambiguity resolution. J Geod 96(2):1–18.

[17] Pan, L.; Xiong, B.; Li, X.; Yu, W.; Dai, W. High-rate GNSS multi-frequency uncombined PPP-AR for dynamic deformation monitoring. Adv. Space Res. 2023, 72, 4350–4363.

[18] Wübbena G, Schmitz M, Bagge A (2005) PPP-RTK: precise point positioning using state-space reprentation in RTK networks. In: Proceedings of ION GNSS-2005, Long Beach, CA, pp 2584–2594.

[19] Li X, Zhang X, Ge M (2011). Regional reference network augmented precise point positioning for instantaneous ambiguity resolution. J Geodesy 85(3):151–158.

[20] Li X, Ge M, Dousa J, Wickert J (2014) Real-time precise point positioning regional augmentation for large GPS reference networks. GPS Solution 18(1):61–71.

[21] Li, X., Huang, J., Li, X. et al (2022). Review of PPP–RTK: achievements, challenges, and opportunities. Satellite Navigation 3, 28.

[22] Teunissen P, Odijk D, Zhang B (2010). PPP-RTK: results of CORS network-based PPP with integer ambiguity resolution. J Aeronaut, Astronaut Aviat 42(4):223–230.

[23] Odijk D, Zhang B, Khodabandeh A, Odolinski R, Teunissen PJ (2016) On the estimability of parameters in undifferenced, uncombined GNSS network and PPP-RTK user models by means of S-system theory. J Geod 90(1):15–44.

[24] Khodabandeh A, Teunissen P (2014) Array-based satellite phase bias sensing: theory and GPS/BeiDou/QZSS results. Meas Sci Technol 25(9):095801.

[25] Cui, B.; Jiang, X.; Wang, J.; Li, P.; Ge, M.; Schuh, H. A new large-area hierarchical PPP-RTK service strategy. GPS Solut. 2023, 27, 134.

[26] Odijk D, Teunissen PJ, Zhang B (2012) Single-frequency integer ambiguity resolution enabled GPS precise point positioning. J Surv Eng 138(4):193–202.

[27] Li X, Han J, Li X, Huang J, Shen Z, Wu Z (2023) A grid-based ionospheric weighted method for PPP-RTK with diverse network scales and ionospheric activity levels. GPS Solut 27(4):191

[28] Khodabandeh, A., & Teunissen, P. J. G. (2016). PPP–RTK and inter-system biases: The ISB look-up table as a means to support multi-system PPP–RTK. Journal of Geodesy, 90, 837–851.

[29] Li, X., Huang, J., Li, X., Lyu, H., Wang, B., Xiong, Y., & Xie, W. (2021). Multi-constellation GNSS PPP instantaneous ambiguity resolution with precise atmospheric corrections augmentation. GPS Solutions, 25(3), 1–13.

[30] Ma, H., Psychas, D., Xing, X., Zhao, Q., & Liu, X. (2021). Influence of the inhomogenous troposphere on GNSS positioning and integer ambiguity resolution. Advances in Space Research, 67(2), 1914–1928.

[31] Li, X., Wang, B., Li, X., Huang, J., Lyu, H., & Han, X. (2022). Principle and performance of multi-frequency and multi-GNSS PPP–RTK. Satellite Navigation, 3(1), 1–11.

[32] Lyu Z, Gao Y (2022) PPP-RTK with augmentation from a single reference station. J Geod 96(6):40.

[33] Hou P, Zhang B, Yasyukevich YV, Liu T, Zha J (2022) Multi-frequency phase-only PPP-RTK model applied to BeiDou data. GPS Solut 26:76.

[34] Psychas, D., Teunissen, P. J. G., & Verhagen, S. (2021). A multi-frequency Galileo PPP–RTK convergence analysis with an emphasis on the role of frequency spacing. Remote Sensing, 13, 3077.

[35] Zhang, B., Hou, P., Zha, J. et al (2022). PPP–RTK functional models formulated with undifferenced and uncombined GNSS observations. Satell Navigation 3, 3.

[36] Zhang, B., Chen, Y., & Yuan, Y. (2019). PPP–RTK based on undifferenced and uncombined observations: Theoretical and practical aspects. Journal of Geodesy, 93(7), 1011–1024.

[37] Zhang, B., Liu, T., & Yuan, Y. (2018). GPS receiver phase biases estimable in PPP–RTK networks: Dynamic characterization and impact analysis. Journal of Geodesy, 92(6), 659–674.

[38] Wang, K., Khodabandeh, A., & Teunissen, P. (2017). A study on predicting network corrections in PPP–RTK processing. Advances in Space Research, 60(7), 1463–1477.

[39] Zhang, X., Ren, X., Chen, J. et al (2022). Investigating GNSS PPP–RTK with external ionospheric constraints. Satell Navigation 3, 6.

[40] Ge M, Gendt G, Rothacher M, Shi C and Liu J (2005). Resolution of GPS carrier-phase ambiguities in precise point positioning (PPP) with daily observations J. Geod. 82 389–99.

[41] Mervart L, Lukes Z, Rocken C and Iwabuchi T (2008). Precise point positioning with ambiguity resolution in real-time Proc. 21st Int. Technical Meeting of the Satellite Division of The Institute of Navigation, ION GNSS (Savannah, GA).

[42] Laurichesse D, Mercier F, Berthias J, Broca P and Cerri L (2009). Integer ambiguity resolution on undifferenced GPS phase measurements and its application to PPP and satellite precise orbit determination J. Inst. Navig. 56 135–49.

[43] Ge M, Gendt G, Rothacher M, Shi C and Liu J (2005). Resolution of GPS carrier-phase ambiguities in precise point positioning (PPP) with daily observations J. Geod. 82 389–99.

[44] B. Parkinson, P. Enge (2005). Differential GPS. In: Global Positioning System: Theory and Applications, Vol. 2, ed. by B. Parkinson, J.J. Spilker Jr. (AIAA, Washington) pp. 3–50.

[45] G. Wübbena, A. Bagge, G. Seeber, V. Böder, P. Hankemeier (1996). Reducing distance dependent errors for real-time precise DGPS applications by establishing stations networks, Proc. ION GPS-96, Kansas City (ION, Virginia) pp. 1845–1852.

[46] C. Kee, B.W. Parkinson (1996). Wide area differential GPS (WADGPS): Future navigation system, IEEE Trans. Aerosp. Electron. Syst. 32(2), 795–808.

[47] Liu X, de Jong K, Tiberius C (2003). Reparameterization of single difference and undifferenced kinematic GPS positioning models. Geo-Spatial Information Science, 6(2), 1-7.

[48] Mi X, Zhang B, Yuan Y (2019). Stochastic modeling of between-receiver single-differenced ionospheric delays and its application to medium baseline RTK positioning. Measurement Science and Technology 30:095008.

[49] Liu X, Tiberius C, de Jong K (2004). Modelling of differential single difference receiver clock bias for precise positioning. GPS Solutions, 7(4), 209-221.

[50] Odolinski R, Teunissen P, Odijk D (2015a). Combined GPS + BDS for short to long baseline RTK positioning. Measurement Science and Technology.26 045801.

[51] Tian Y, Yuan L, Tan L, Yan H, Xu S (2019). Regularization and particle filtering estimation of phase inter-system biases (ISB) and the lookup table for Galileo E1-GPS L1 phase ISB calibration. GPS Solutions 23.

[52] Odolinski R, Teunissen P, Odijk D (2015b). Combined BDS, Galileo, QZSS and GPS single-frequency RTK. GPS Solutions 19:151-163.

[53] Odijk D, Nadarajah N, Zaminpardaz S, Teunissen PJG (2017). GPS, Galileo, QZSS and IRNSS differential ISBs: estimation and application. GPS Solutions 21:439-450.

[54] X. Li, Y. Tan, Z. Shen, X. Li and Y. Zhou (2024). "GNSS-Based Cooperative Instantaneous Precise Positioning Aided by Multi-Epoch and Multi-Agent Associations," in IEEE Transactions on Vehicular Technology, vol. 73, no. 6, pp. 7771-7784.

[55] Marques, H. A. Monico, J. F. G. Aquino, M. (2011). RINEX_HO: second- and third-order ionospheric corrections for RINEX observation files. GPS Solutions. 15, p. 305-314.

[56] Schüler, T., Diessongo, H. & Poku-Gyamfi, Y (2011). Precise ionosphere-free single-frequency GNSS positioning. GPS Solut 15, 139–147.

[57] Odijk, D. (2003). Ionosphere-free phase combinations for modernized GPS. Journal of surveying engineering, 129(4), 165-173.

[58] Zhang, B., Hou, P., Liu, T., & Yuan, Y. (2020). A single-receiver geometry-free approach to stochastic modeling of multi-frequency GNSS observables. Journal of Geodesy, 94, 1-21.

[59] Feng, W., Zhao, Y., Zhou, L., Huang, D., & Hassan, A. (2020). Fast cycle slip determination for high-rate multi-GNSS RTK using modified geometry-free phase combination. Gps Solutions, 24, 1-11.

[60] Cui, B., Li, P., Wang, J., Ge, M., & Schuh, H. (2021). Calibrating receiver-type-dependent wide-lane uncalibrated phase delay biases for PPP integer ambiguity resolution. Journal of Geodesy, 95(7), 82.

[61] Duong, V., Harima, K., Choy, S., Laurichesse, D., & Rizos, C. (2020). An assessment of wide-lane ambiguity resolution methods for multi-frequency multi-GNSS precise point positioning. Survey Review.

[62] Atiz, O. F., Ogutcu, S., Alcay, S., Li, P., & Bugdayci, I. (2021). Performance investigation of LAMBDA and bootstrapping methods for PPP narrow-lane ambiguity resolution. Geo-Spatial Information Science, 24(4), 604-614.

[63] Zheng, K., Tan, L., Liu, K., Li, P., Chen, M., & Zeng, X. (2023). Multipath mitigation for improving GPS narrow-lane uncalibrated phase delay estimation and speeding up PPP ambiguity resolution. Measurement, 206, 112243.

[64] Zhang B, Teunissen P, Odijk D (2011) A novel un-differenced PPP-RTK concept. J Navig 64(S1): S180–S191

[65] Zhang, B., Hou, P., & Odolinski, R. (2022). PPP-RTK: from common-view to all-in-view GNSS networks. Journal of Geodesy, 96(12), 102.

[66] Ke, C., Zhang, B., & Khodabandeh, A. (2024). Extension of the undifferenced and uncombined CDMA PPP-RTK for not-common-frequency GNSS observations. GPS Solutions, 28(3), 102.

[67] Geng, J., Zeng, R. & Guo, J. Assessing all-frequency GPS/Galileo/BDS PPP-RTK in GNSS challenging environments. GPS Solut 28, 5 (2024).

[68] Wang, F., & Zhang, K. (2023). All-Frequency GNSS PPP-RTK Using Observable-Specific Signal Biases for Urban Environments. In Proceedings of the 36th International Technical Meeting of the Satellite Division of the Institute of Navigation (ION GNSS+ 2023) (pp. 2682-2697).

[69] Ma, H., Zhao, Q., Verhagen, S., Psychas, D., & Liu, X. (2020). Assessing the performance of multi-GNSS PPP-RTK in the local area. Remote sensing, 12(20), 3343.

[70] Nadarajah, N., Khodabandeh, A., Wang, K., Choudhury, M., & Teunissen, P. J. (2018). Multi-GNSS PPP-RTK: from large-to small-scale networks. Sensors, 18(4), 1078.

[71] Psychas, D., & Verhagen, S. (2020). Real-Time PPP-RTK Performance Analysis Using Ionospheric Corrections from Multi-Scale Network Configurations. Sensors, 20(11), 3012.

[72] Wang, S.; Li, B.; Gao, Y.; Gao, Y.; Guo, H. A comprehensive assessment of interpolation methods for regional augmented PPP using reference networks with different scales and terrains. Measurement 2020, 150, 107067.

[73] Zhang, B., Hou, P., Zha, J., & Liu, T. (2021). Integer-estimable FDMA model as an enabler of GLONASS PPP–RTK. Journal of Geodesy, 95(8), 1–21.

[74] Zha, J., Zhang, B., Liu, T., & Hou, P. (2021). Ionosphere-weighted undifferenced and uncombined PPP–RTK: Theoretical models and experimental results. GPS Solutions, 25(4), 1–12.

[75] Wang K, EI-Mowafy A, Qin W, Yang X (2022) Integrity monitoring of PPP-RTK positioning; part I: GNSS-based IM procedure. Rem Sens 14(1):44.

[76] Zhang W, Wang J (2023) Integrity monitoring scheme for single-epoch GNSS PPP-RTK positioning. Satell Navig 4:10-68.

[77] Zhang W, Wang J, El-Mowafy A, Rizos C (2023) Integrity monitoring scheme for undifferenced and uncombined multi-frequency multi-constellation PPP-RTK. GPS Solut 27(2):68.

[78] Wang S, Zhan X, Zhai Y, Gao Z (2023) solution separation-based integrity monitoring for integer ambiguity resolution-enabled GNSS positioning. In: Proceedings of the 2023 international technical meeting of the institute of navigation, Long Beach, California, pp 492–513.

[79] Lyu S, Xiang Y, Soja B, Wang N, Yu W, Truong TK (2023) Uncertainties of interpolating satellite-specific slant ionospheric delays and impacts on PPP-RTK. IEEE Trans Aerosp Electron Syst 60(1):490–505.

[80] Bartier, P. M., & Keller, C. P. (1996). Multivariate interpolation to incorporate thematic surface data using inverse distance weighting (IDW). Computers & Geosciences, 22(7), 795-799.

[81] Oliver, M. A., & Webster, R. (1990). Kriging: a method of interpolation for geographical information systems. International Journal of Geographical Information System, 4(3), 313-332.

[82] Moritz, H. (1978). Least‐squares collocation. Reviews of geophysics, 16(3), 421-430.

[83] Nurunnabi, A., Belton, D., & West, G. (2014). Robust statistical approaches for local planar surface fitting in 3D laser scanning data. ISPRS journal of photogrammetry and Remote Sensing, 96, 106-122.

[84] Teunissen, P. J. G. (1985). Generalized inverses, adjustment, the datum problem and S-transformations. In E. W. Grafarend & F. Sanso (Eds.), Optimization of Geodetic Networks. Springer.

[85] Hofmann-Wellenhof, B., Lichtenegger, H., & Wasle, E. (2007). GNSS–global navigation satellite systems: GPS, GLONASS, Galileo, and more. Springer Science & Business Media.

[86] Kleusberg, A., & Teunissen, P. J. (1996). GPS for Geodesy (Vol. 60). Berlin: Springer.

[87] Saastamoinen, J. (1972). Atmospheric correction for the troposphere and stratosphere in radio ranging satellites. The use of artificial satellites for geodesy, 15, 247-251.

[88] Böhm, J., Möller, G., Schindelegger, M., Pain, G., & Weber, R. (2015). Development of an improved empirical model for slant delays in the troposphere (GPT2w). GPS solutions, 19, 433-441.

[89] Teunissen, P. J., De Jonge, P. J., & Tiberius, C. C. J. M. (1997). Performance of the LAMBDA method for fast GPS ambiguity resolution. Navigation, 44(3), 373-383.

[90] Kouba, J., & Héroux, P. (2001). Precise point positioning using IGS orbit and clock products. GPS solutions, 5, 12-28.

[91] Wu, J. (1994). The sea surface is aerodynamically rough even under light winds. Boundary-layer meteorology, 69(1), 149-158.

[92] Yang, Y., & Gao, W. (2006). An optimal adaptive Kalman filter. Journal of Geodesy, 80, 177-183.

[93] Y. Yang, L. Song and T. Xu (2002). "Robust estimator for correlated observations based on bifactor equivalent weights", *J. Geodesy*, vol. 76, no. 6, pp. 353-358.

[94] Renka R. J. and Brown R. (1999). Accuracy tests of ACM algorithms for interpolation of scattered data in the plane, ACM Transactions on Mathematical Software. 25, no. 1, 78–94

[95] Fleit, G. Windowed anisotropic local inverse distance-weighted (WALID) interpolation method for riverbed mapping. Acta Geophys. 73, 2819–2833 (2025).

[96] Moritz H (1976). Covariance Functions in Least-Squares Collocation. The Ohio State University, Department of Geodetic Science; Columbus, OH, USA: 1976. Reports of the Department of Geodetic Science, Report No. 240.

[97] Teunissen P.J.G (2007). Least-squares prediction in linear models with integer unknowns. J. Geod.;81:565–579.

[98] Goldberger A (1962). Best linear unbiased prediction in the generalized linear regression model. J. Am. Stat. Assoc; 57:369–375.